Any correspondence concerning this service should be sent to the repository administrator: tech-oatao@listes-diff.inp-toulouse.fr

# Double seismic zone of the Nazca plate in northern Chile: High-resolution velocity structure, petrological implications, and thermomechanical modeling

**Catherine Dorbath**
*IRD UR154 and EOST, Université Louis Pasteur, F-67084 Strasbourg, France (catherine.dorbath@eost.u-strasbg.fr)*

**Muriel Gerbault**
*IRD UR154, Departamento de Geologia, Universidad de Chile, Santiago, Chile*

*Also at LMTG, UMR5563, CNRS, F-31400 Toulouse, France*

**Gabriel Carlier and Michel Guiraud**
*Minéralogie-Pétrologie, UMR7160, CNRS, and USM 201, MNHN, F-75005 Paris, France*

[1] This paper presents an interdisciplinary study of the northern Chile double seismic zone. First, a high-resolution velocity structure of the subducting Nazca plate has been obtained by the tomoDD double-difference tomography method. The double seismic zone (DSZ) is observed between 80 and 140 km depth, and the two seismic planes is 20 km apart. Then, the chemical and petrologic characteristics of the oceanic lithosphere associated with this DSZ are deduced by using current thermal-petrological-seismological models and are compared to pressure-temperature conditions provided by a numerical thermomechanical model. Our results agree with the common hypothesis that seismicity in both upper and lower planes is related to fluid releases associated with metamorphic dehydration reactions. In the seismic upper plane located within the upper crust, these reactions would affect material of basaltic (MORB) composition and document different metamorphic reactions occurring within high-P (>2.4 GPa) and low-T (<570°C) jadeite-lawsonite blueschists and, at greater depth (>130 km), lawsonite-amphibole eclogite conditions. The lower plane lying in the oceanic mantle can be associated with serpentinite dehydration reactions. The Vp and Vs characteristics of the region in between both planes are consistent with a partially ($\sim25-30$ vol % antigorite, $\sim0-10\%$ vol % brucite, and $\sim4-10$ vol % chlorite) hydrated harzburgitic material. Discrepancies persist that we attribute to complexities inherent to heterogeneous structural compositions. While various geophysical indicators evidence particularly cold conditions in both the descending Nazca plate and the continental fore arc, thermomechanical models indicate that both seismic planes delimit the inner slab compressional zone around the 400°C (±50°C) isotherm. Lower plane earthquakes are predicted to occur in the slab's flexural neutral plane, where fluids released from surrounding metamorphic reactions could accumulate and trigger seismicity. Fluids migrating upward from the tensile zone below could be blocked in their ascension by the compressive zone above this plane, thus producing a sheeted layer of free fluids, or a serpentinized layer. Therefore earthquakes may present either downdip compression and downdip tensile characteristics. Numerical tests indicate that the slab's thermal structure is not the only factor that controls the occurrence of inner slab compression. (1) A weak ductile subduction channel and (2) a cold mantle fore arc both favor inner slab compression by facilitating transmission of compressional stresses from the continental lithosphere into the slab. (3) Decreasing the radius of curvature of the slab broadens the depth of inner slab compression, whereas (4) decreasing upper plate convergence diminishes its intensity. All these factors indicate that if DSZs indeed contour inner slab compression, they cannot be

linked only to slab unbending, but also to the transmission of high compressional stresses from the upper plate into the slab.

## 1. Introduction

[2] Since *Hasegawa et al.* [1978] showed the existence of a double-planed deep seismic zone in the northern Japan arc, more and more double seismic zones (DSZ) have been recognized in worldwide subduction zones like Tonga, New Britain, Kuriles, Kamchatka, Aleutians or Alaska [*Peacock*, 2001]. Actually, a recent analysis of various subducting plates reveals the global prevalence of DSZ, which were found in segments of 16 subduction zones [*Brudzinski et al.*, 2007]. For these zones, the intermediate depth earthquakes (80 to 180 km) define two dipping planes separated by a distance increasing with plate age, from ∼8 km for a ∼12-Ma-old slab to ∼30 km for a 160-Ma-old slab.

[3] Seismicity in both upper and lower seismic zones occurs where stable hydrous minerals are predicted [*Hacker et al.*, 2003b]. Upper plane seismicity is linked to dehydration of metabasalts from the oceanic crust, and lower plane seismicity would be promoted by dehydration embrittlement of serpentinized mantle, e.g., antigorite [*Hacker et al.*, 2003b; *Yamasaki and Seno*, 2003; *Brudzinski et al.*, 2007], with mantle hydration acquired by infiltration of seawater through outer rise faults prior to subduction [*Seno and Yamanaka*, 1996; *Peacock*, 2001].

[4] Despite this observation of a first-order dependency of DSZ separation on plate age by *Brudzinski et al.* [2007], the mechanical cause for their occurrence remains misunderstood. Numerous authors have suggested that DSZs are caused by unbending of the lithosphere after passing the position of maximum curvature [e.g., *Engdahl and Scholz*, 1977; *Isacks and Barazangi*, 1977; *Wang*, 2002],

inducing upper plane compressional earthquakes in the top part of the slab, and lower plane downdip tension earthquakes in its bottom part. But many slabs are nearly planar where the lower plane seismicity continues [e.g., *Fujita and Kanamori*, 1981; *Abers*, 1992], suggesting that a continuous stress acts on the slab long after it has passed the point of unbending. Fault plane solutions are also found poorly consistent with plate bending and unbending about a neutral fiber [e.g., *Peacock*, 2001]. A while ago, *Fujita and Kanamori* [1981] had suggested that double seismic zones are observed in slabs for which the plate sinking rate (function of its age) differs from surface plate convergence velocity, sufficiently to generate stress-segmented seismic zones. When such slabs are on average, neither dominantly in tension or compression, seismogenic deviatoric stresses may be generated by local factors such as, for example, thermal stresses or compressional stresses transmitted from the upper plate into the slab.

[5] It is known that a double seismic zone also exists in the subducting Nazca plate beneath northern Chile, just south of the Arica elbow. Yet, seismic data lead controversial DSZ characteristics. In this area, the 50 Ma old Nazca plate [e.g., *Cande and Haxby*, 1991] is subducting beneath the South American plate at a rate of 84 mm/a. From a microseismic field experiment between 20 and 24°S, *Comte and Suarez* [1994] observed, at depths of 80 to 150 km, two families of events with opposite focal mechanisms; the average separation between these two sets of events is about 15 km, suggesting a double layered slab. Nevertheless, the high-quality results from the PISCO'94 experiment, deployed in the same region, gave no evidence for a double seismic zone [*Graeber and Asch*, 1999]. On the other hand, locally recorded

events between 18.5 and 19.5°S display, at depths greater than 100 km, two distinct planes separated by 20 to 25 km, with an extreme variability of the focal mechanisms observed in both planes [*Comte et al.*, 1999]. About 300 km south, around 22°S, *Rietbrock and Waldhauser* [2004] used the double-difference algorithm (hypoDD [*Waldhauser*, 2001]) to evidence a 9 km thick DSZ at 80–130 km depth, and with predominant extensional events in both upper and lower planes.

[6] Recently, *Zhang et al.* [2004] provided high-resolution constraints on the petrological processes involved in double seismic zones by studying the subduction beneath northern Honshu, using an improved double-difference tomography method, tomoDD. Where previous seismic tomography studies lack information, particularly on the velocity structure of the deeper part of the slabs, this method is able to produce more accurate velocity images in the region near the sources [*Zhang and Thurber*, 2003]. In this paper, we first apply this new double-difference tomography code to the Arica zone data (section 2.1), to obtain a detailed velocity model of the subducting Nazca plate where a double seismic zone has been observed (section 2.2). From this velocity model we then compare our results with those obtained for Honshu, and discuss the implications on petrological compositions when using *Hacker and Abers* [2004] calculation scheme (section 2.2). Among these peculiar implications, we argue for a cold thermal environment, and therefore develop in section 3 a thermomechanical numerical model of the northern Chile subduction zone. We start this section 3 by reviewing the literature, surface heat fluxes, thermal models and geophysical data of the area (section 3.1). We then expose our numerical approach, with initial conditions that are based on these data, and results that display the evolution of the subduction zone toward a transient thermomechanical state (section 3.2) that accounts for elastic-viscous and brittle behavior. We then reconsider our initial petrological results in comparison to the pressure-temperature conditions obtained with these thermomechanical models (section 3.3), and finally display alternate thermomechanical models, in which we show that not only temperatures but also stresses play a crucial role in the width and depth of DSZs (section 3.4). This paper is consequently rather dense as it contains a number of interdisciplinary considerations, but it is also this interdisciplinary approach that provided us with a global view of the processes in play, allowing to frame the peculiar conclusions we propose.

## 2. High-Resolution Velocity Structure

### 2.1. Data and Method

[7] From June to August 1996, a dense temporary seismic network was deployed in the Arica region from the coast to the Bolivian border, between the Peruvian border and 19°20′S. This short period array of 24 vertical and 10 three-component stations complemented the Arica permanent network of 9 stations (Figure 1). P and S arrival times in these 43 stations were used to determine hypocentral locations. A description of the network and location process is given by *Comte et al.* [1999]. In this paper, only the travel times of the very best located earthquakes recorded during this experiment, complemented by those recorded by the permanent network from January 1996 to December 1997, have been used.

[8] We kept 2052 events, which met all the following restrictive criteria: number of readings higher than 10 including 2 S, distance to the nearest station lower than depth, RMS lower than 0.25, azimuthal gap lower than 300 and conditioning factor lower than 100 (Figure 1). We preferred using these few very selected events instead of numerous redundant and poorly located events that will introduce noise in the data and degrade the results. We obtained about 36,000 absolute travel times (~55% of P waves), from which we constructed 171,000 differential travel times for events pairs. We used the same interevent maximal distance as *Zhang et al.* [2004], e.g., 10 km at common stations, in order to reduce the velocity model dependency on double-difference earthquake relocation.

[9] In addition to the hypocentral relocations, we simultaneously solve the P and S wave velocity structure at each grid node. The chosen inversion grid is presented on Figure 1 in map view. The origin of the grid is at X = 69°W, Y = 18°S, Z = 0 km. Rotation of the reference frame to N77°E corresponds to the convergence direction of the Nazca plate underneath South America at that latitude. The distance between nodes is 10 km in the three directions, down to 160 km, below the maximal depth of the hypocenters in this area. We first inverted these travel times data for a 1-D velocity model, starting from the very simple model previously used for the standard hypocentral location procedure in northern Chile (in blue in
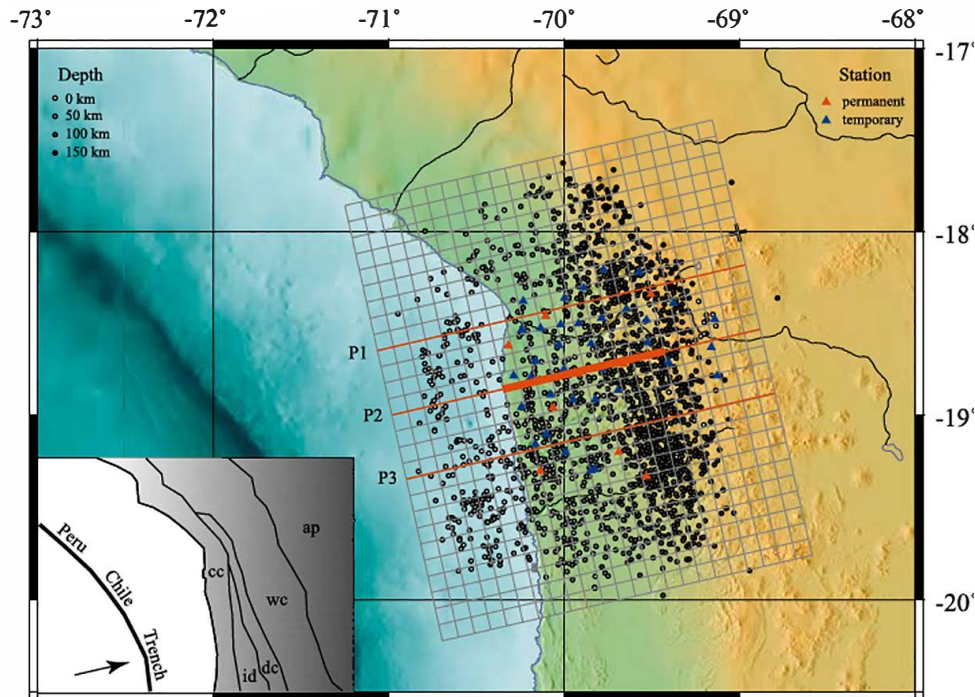
**Figure 1.** Epicenters of the 2052 events used in the tomography, the darker, the deeper. Red and blue triangles are stations. The inversion grid used for the inversion is shown in gray. The black cross is the origin of the model (18°S, 69°W). Thin red lines locate the three profiles P1, P2, and P3 presented in Figure 3, and the thick red line indicates the cross section location shown in Figure 4. Insert shows the central Andes tectonic setting between 17° and 20.5°S, modified from *Tassara* [2005]. cc, Coastal Cordillera; id, Intermediate Depression; dc, Domeyko Cordillera; wc, Western Cordillera; ap, Altiplano. Black vector shows Nazca plate absolute motion.

Figure 2), and interpolating it in 17 regularly spaced layers defined between 0 and 160 km. The final model (in red in Figure 2) is very close to the model obtained in the same geographic area by *Comte et al.* [2004] from a 1-D inversion of 10,000 events recorded by 13 stations. In particular, the high-velocity zone at ~50 km depth and the low-velocity zone between 120 and 150 km are observed on both models. The obtained velocities were used as initial velocities for the 3-D tomoDD inversion.

[10] Numerous tests have been performed to check the robustness of the 3-D solution. As we ran tomoDD in LSQR mode, we controlled the damping at each iteration by keeping the condition number value between 40 and 50 [*Waldhauser*, 2001]. Various interevent maximum distances have been tested, and show that inversions using different cutoffs give similar results. Several inversions were performed with various strategies of weighting absolute data relatively to differential data. Our final weighting scheme first a priori downweights the differential data, in order to obtain a large-scale velocity model from the absolute data. In a second step, we favor the differential data, in order to improve the location of nearby events and refine the velocity model. In the last set of iterations, we then reweight the data, according to misfit and event separation, in order to remove or downweight outliers. Various distances between the grid nodes have been tested in order to get the best trade-off between grid spacing and data resolution. The check of the robustness of the solution is presented in Appendix A, and three resolution tests are presented in Appendix B.

## 2.2. Tomography Results and Discussion

[11] We present in Figure 3 three cross sections through our final velocity models Vp and Vs and through the relocated hypocenters along profiles P1 (Y = 20 km), P2 (Y = 60 km) and P3 (Y = 100 km) (Figure 1). These sections are representative of the slab in northern Chile, as other cross sections show similar features. Figure 4 displays Vp and Vs zoomed on the DSZ along profile P2, which is in the center of the studied area and thus the best resolved. In Figures 3 and 4, the white lines correspond to the isovalue 10 of the square
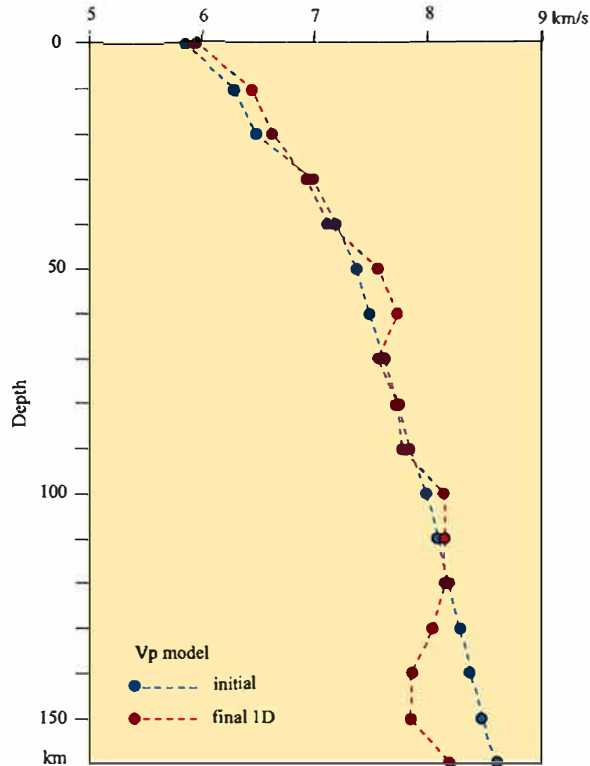
**Figure 2.** Initial layered model (blue) and final Vp model (red) obtained by 1-D inversion.

root of derivative weight sum, considered as the limit for resolved structures. The Vp/Vs model can be obtained by simple division of Vp by Vs models in regions where both models are resolved. Figures A1a and A1b show that the resolution of both models allows to calculate it. However, it is important to keep in mind that such direct division can carry instabilities.

[12] At intermediate depth (80–140 km) the double seismic zone is situated under our seismic array, well defined and reasonably well resolved. Both seismically active planes are 5 to 10 km thick, with a clear separation of 20 km (Figure 3). In this part of the velocity model (Figure 4), the planes present outstanding distinct features which are summarized in Table 1.

### 2.2.1. Fore-Arc Mantle

[13] In the fore-arc mantle below about 40 km and above ~110 km depths, Vp values are in the 7.5– 8 km/s range, and Vs values are in between 4 and 4.5 km/s, very similar to the Honshu region. The Vp/Vs values do not present any large size anomaly, but oscillate from about 1.75 to 1.85. In contrast, in the Honshu region between 20 and 90 km depth below the volcanic arc, Vp/Vs values
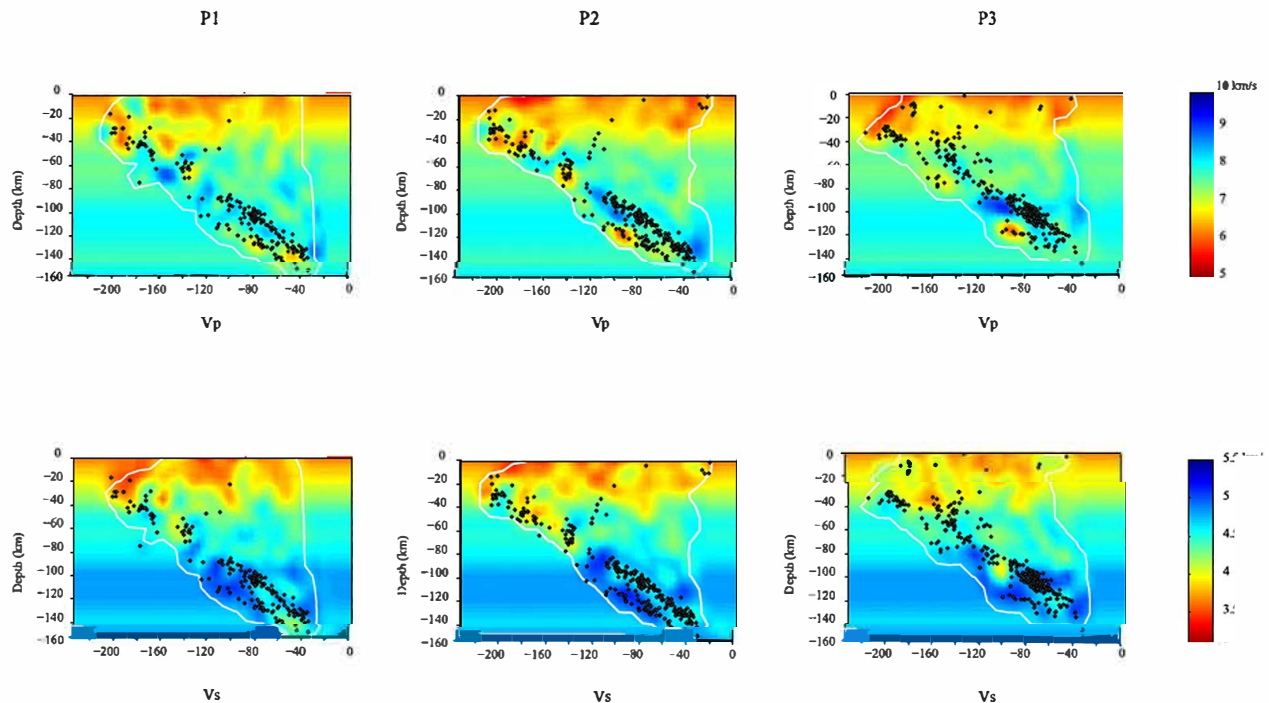


**Figure 3.** Cross section through the Vp and Vs values along the three profiles shown in Figure 1. Plotted earthquakes are within a 20 km wide section. At depths 80–140 km, the double seismic zone is well defined. Both seismic planes are 5 to 10 km thick with a separation of 20 km. Structures above the white line, where derivative weight sum for each node is more than 10, are meaningful.
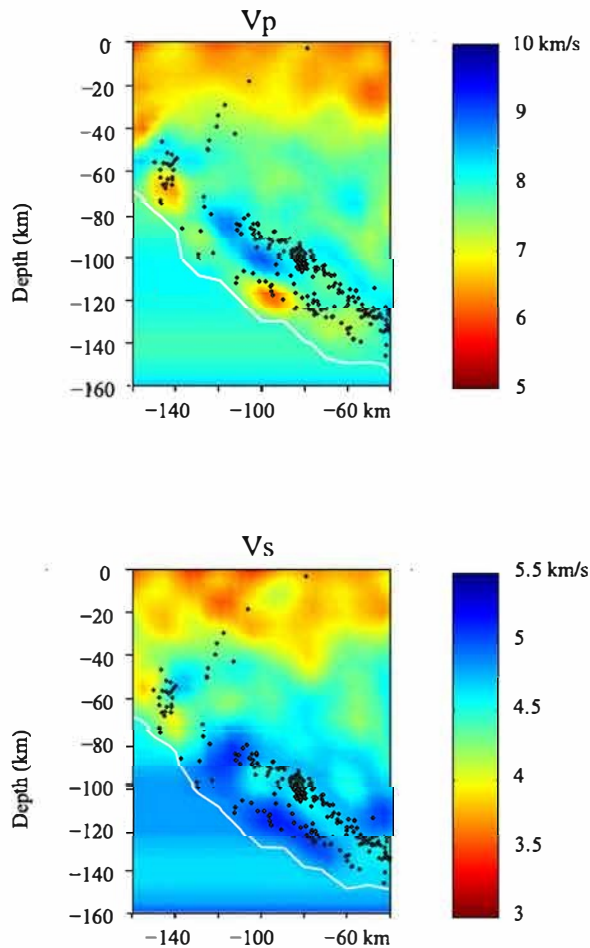
**Figure 4.** Zoom on the velocity structure of the DSZ: cross sections through the Vp and Vs values in the central part of profile P2 (Y = −60 km).

are homogeneously high (∼1.8–1.9), and are interpreted by *Zhang et al.* [2004] to be associated with melt and water inclusions transported through hydraulic fractures from the slab where dehydration reactions occur. These dehydration reactions are attributed to the occurrence of serpentinized peridotite containing melt-filled pores, and are consistent with thermal studies of the Honshu region indicating temperatures above ∼700°C. In northern Chile, however, several studies indicate that the fore-arc mantle is significantly colder, such as thermal models by *Honda* [1985] or *Springer* [1999], and flexural rigidity estimations by *Tassara* [2005] and *Tassara et al.* [2007]. In addition, geophysical studies show an exceptionally low seismic attenuation [e.g., *Haberland et al.*, 2003] (more details in the thermal structure section 3.2), and a specific seismic anisotropy pattern [*Kneller et al.*, 2005, 2007] (details in section 3.2), also

indicative of low temperature and high-stress environment. Therefore, many lines of evidence show that the northern Chile forearc mantle differs from other warm subduction zones that are characterized by extensively serpentinized, melt-equilibrated fore-arc mantle [e.g., *Kelemen et al.*, 2003; *Hyndman and Peacock*, 2003] (see also discussion in section 3.3).

[14] The geological evolution of the south Peruvian and north Chilean fore arc is complex as indicated by the occurrence of Precambrian blocks (i.e., Arequipa Massif) preserved within predominantly volcanic Phanerozoic material. Thus, the fore-arc mantle is probably also complex and predominantly composed of more or less metasomatized harzburgitic material, for which general compositions systematically lead to high Vp (>8. km/s) and Vs (>4.6 km/s) values. At depths of 40–110 km, our recorded velocity values (Vp = 7.5–8.0 km/s; Vs = 4.0–4.5 km/s) militate for a partially hydrated harzburgitic fore-arc mantle, when deduced from petrological simulations (1.2–2.9% $H_2O$, 10–24% modal antigorite [*Hacker et al.*, 2003a; *Hacker and Abers*, 2004]). These petrological simulations are also consistent with the presence of a cold mantle in northern Chile (<600°C).

## 2.2.2. DSZ: Petrological Candidates Deduced From Tomographic Results

[15] Our results (Table 1) are very close to the slab velocity structure obtained by *Zhang et al.* [2004] in the Honshu DSZ at 39°N, and slightly different from those obtained by *Shelly et al.* [2006] at 37°N. In Honshu, the old (130 Ma) Pacific plate subducts beneath the Eurasian plate at 91 mm/a [*DeMets et al.*, 1990]. The two seismic planes of the DSZ are separated by ∼30 km at intermediate depths of 50–140 km.

[16] In New Zealand, the observed DSZ are not as clear as in Japan, however the velocity structure obtained by *Zhang* [2003] with tomoDD in the Wellington region, may be compared to the Chilean results. Nevertheless in this region, the Pacific

**Table 1.** Vp and Vs Values and Vp/Vs Ratios in the Nazca Plate DSZ Obtained in This Study

|                   | Vp (km/s) | Vs (km/s) | Vp/Vs |
|-------------------|-----------|-----------|-------|
| Upper plane       | 7.7       | 4.6       | ∼1.67 |
| Region in between | 8.5       | 4.5       | ∼1.89 |
| Lower plane       | 7.4       | 4.7       | ∼1.57 |

**Table 2.** Vp and Vs Values and Vp/Vs Ratios Obtained by tomoDD in Other DSZ[a]

| Region | Vp (km/s) | | Vs (km/s) | | Vp/Vs | |
|---|---|---|---|---|---|---|
| Upper plane | | | | | | |
| Honshu 39°N | 7.8 | 8.0 | 4.4 | 4.5 | 1.72 | 1.85 |
| Honshu 37°N | 8.5 | | | | 1.82 | |
| New Zealand 41°S | 7.5 | | | | 1.65 | |
| Region in between | | | | | | |
| Honshu 39°N | 8.2 | 8.4 | 4.6 | | 1.8 | 1.85 |
| Honshu 37°N | | | | | | |
| New Zealand 41°S | 8.5 | | | | 1.9 | |
| Lower plane | | | | | | |
| Honshu 39°N | 7.6 | 7.8 | 4.7 | 4.9 | 1.6 | 1.7 |
| Honshu 37°N | 8.0 | | | | 1.7 | |
| New Zealand 41°S | 7.0 | 7.5 | | | 1.55 | |

[a] Honshu 39°N [*Zhang et al.*, 2004], Honshu 37°N [*Shelly et al.*, 2006], and New Zealand 41°S [*Zhang*, 2003].

plate is about 120 Ma old, and the subduction process is much slower (42 mm/a). Both seismic planes are detected at shallower depths, from 50 km to only 80 km because of land-sea limits, and are separated by ~10 km. The results of these three tomoDD studies are summarized in Table 2. The structure of the Hikurangi subduction zone beneath the central North Island, New Zealand, to the north of Zhang's study [*Reyners et al.*, 2006] was also obtained by simultaneous inversion for both hypocenters and the 3-D Vp and Vp/Vs structure [*Thurber*, 1983, 1993]. Results define the DSZ down to 130–140 km depth. Earthquakes in the lower plane are generally associated with regionally high Vp values, and a specifically low Vp/Vs, which is similar to lower plane earthquakes in northern Honshu.

[17] Focal mechanisms would help identifying the physical processes and metamorphic reactions involved in northern Chile DSZ. Focal mechanisms constructed for the events recorded during the 1996 campaign have been presented by *Comte et al.* [1999]. For the present study, we used our relocated events to construct focal mechanisms when possible. Only 45 solutions were constrained, among which 41 located in the upper plane, and 4 remaining in the lower plane. Our results do not differ from those obtained by *Comte et al.* [1999]: fault plane solutions for these intermediate depth events vary significantly, even between nearby events. The very few events associated with the lower subduction plane also present an extreme variability (with both tensional and compressional mechanisms). Finally, polarities read from the very few earthquakes located in between both planes do not enable to draw any reliable mechanism. Such

results were also observed by *Abers* [1992] in the Aleutian DSZ.

[18] In order to assess the petrological compositions consistent with our tomographic data, the velocities proposed and discussed hereafter have been computed by averaging the values obtained in the central part of our model for the same area of the DSZ (upper plane, lower plane, and region in between), from P1 to P3 (Figure 1). Mineral rock compositions involved in upper and lower planes, and in between, are obtained by using *Hacker and Abers*'s [2004] procedure. For suitable Vp velocity data, we have selected rock compositions displaying the Vs velocities that most closely approximate the observed data. Then, the results are compared with available, independent petrogenetic data.

### 2.2.3. Upper Plane

[19] The upper plane of earthquakes in northern Chile lies in a region of relatively low Vp (7.7 km/s) and normal Vs (4.6 km/s) values, thus relatively low Vp/Vs ratio (~1.67) (Table 1), from 80 to 130 km depth. Between 80 km (~2.4 GPa) and 140 km (~4.5 GPa) depth and, for rocks of basic composition (MORB), mineral velocities estimated by using the calculation scheme of *Hacker and Abers* [2004] imply mineral assemblages of relatively low Vp and high Vs values and, relatively high Vp and low Vs values, respectively for each depth. Common minerals at such pressure and temperature are coesite, jadeite, kyanite and garnet, that show high Vs (>4.6 km/s) but also high Vp (>7.8 km/s) values. Therefore, whatever their respective modal proportions, these minerals must necessarily be associated with amphibole and/or chlorite, which significantly decrease the bulk rock Vp values. Conversely, the observed low Vp velocity values preclude anhydrous metabasic rocks such as eclogite. Velocity simulations with *Hacker and Abers* [2004] tables agree with this conclusion.

[20] Petrogenetic grids modeling high-pressure metabasic rocks (CNFMASH system + silica phase and $H_2O$ in excess) provide additional constraints [e.g., *Clarke et al.*, 1997; *Carson et al.*, 1999]. In theses systems, at temperatures above 550°C, garnet and clinozoisite occur at the expense of chlorite and lawsonite, respectively. In contrast at low temperatures (<570°C), chlorite coexists with lawsonite, amphiboles and omphacite over a large pressure domain (e.g., lawsonite is stable above 1.6 GPa at 550°C). Since the relatively low Vp values of northern Chile upper seismic plane imply the presence of chlorite and amphibole rather than

garnet and clinozoisite, we propose that the involved mafic metamorphic rocks are characterized by low temperature (<570°C) mineral assemblages in presence of water. Petrological simulations using low temperature (500°C) and lawsonite-omphacite-amphibole-chlorite assemblages with 4.0–5.7 wt % $H_2O$ and, at greater depth, lawsonite amphibole eclogite with 3.0 wt % $H_2O$ [*Hacker and Abers*, 2004], provide Vp values that are close to observations.

[21] Accordingly, we suggest that between 80 and 140 km depths, the seismic upper plane in northern Chile is related to fluid release associated with metamorphic reactions occurring within jadeite-lawsonite blueschists and, at greater depth, under lawsonite-amphibole eclogite conditions. Note that these conditions occur at relatively low temperature (<570°C), consistent with indications of the cold state of the north Chilean subduction zone (see section 3.1).

### 2.2.4. Intermediate Zone

[22] In between both seismic planes of the northern Chile DSZ, mean Vp values are high (8.5 km/s), mean Vs values are slightly low to normal (4.5 km/s), leading a high Vp/Vs ratio (~1.8) (Table 1). Nevertheless, we observe a global decrease of the velocity values with depth, from [Vp ~ 8.8, Vs ~ 4.7] at ~80 km depth, to [Vp ~ 8.3, Vs ~ 4.4] at ~130 km depth. Vp values as high as 8.8 km/s are indicative of unmetamorphosed or metamorphosed harzburgite composition [*Hacker et al.*, 2003a] under very high pressure (above 4.5 GPa for unmetamorphosed harzburgite, above 7 GPa for metamorphosed harzburgite), much greater than those inferred from the lithostatic conditions of the intermediate zone of northern Chile (<3.5 GPa). Simulations using *Hacker and Abers* [2004] indicate that, at 80 km depth and temperature < 500°C, observed mean Vp values are consistent with anhydrous or slightly hydrated harzburgitic material (<0.6 wt % $H_2O$, ~10 vol % antigorite). At 130 km depth, observed Vp values of 8.3 km/s are consistent with a similar material of water content up to 1.2 wt % (~10 vol % antigorite) at low temperature (300°C) and 0.6 wt % (~5 vol % antigorite) at higher temperature (600°C).

### 2.2.5. Lower Plane

[23] In northern Chile, the lower plane of seismicity is characterized at all depths down to 130 km, by low Vp values (7.4 km/s), high Vs values (4.7 km/s), and very low Vp/Vs ratio (~1.57) (Table 1). Similar data have only been reported in the lower plane of Wellington DSZ, New Zealand [*Zhang*, 2003] (Table 2). Such results have been generally attributed to serpentinites or chlorite-bearing harzburgites. However, at depths greater than 80 km (above ~2.5 GPa), occurrence of fully serpentinized rocks (15 wt % $H_2O$) is ruled out because they display too low Vp values (<6.2 km/s) with respect to the observed data of northern Chile. Better results are obtained when partially hydrated harzburgite compositions are considered (5–7 wt % $H_2O$, with ~25–30 vol % antigorite, ~0–10% vol % brucite and ~4–10 vol % chlorite, from petrological simulations). At considered depths and in order to maintain relatively high Vs, such compositions imply that temperature probably does not exceed 500°C in brucite-bearing or, depending on water activity, 500–650°C in brucite-free assemblages [see, e.g., *Hacker et al.*, 2003a; *Perrillat et al.*, 2005].

[24] In conclusion, like for other worldwide DSZs, northern Chile lower plane seismicity can be ascribed to dehydration reactions occurring within partially hydrated harzburgites. As noted above, the most probable involvement of brucite breakdown in these dehydration reactions and the fact that water activity is probably <1, implies that temperatures do not exceed 600°C.

[25] Serious limitations to previous interpretations arise when considering the observed Vs values and Vp/Vs ratios (Table 1). Even worse, no mineral assemblage displaying both observed Vp and Vs values can be simulated using *Hacker and Abers*'s [2004] calculation tables. The simulations systematically result in mineral assemblages displaying higher or lower Vs velocity for a suitable Vp velocity and vice versa. Such discrepancy may be ascribed to various parameters such as the presence of more complex oceanic crust or mantle compositions, occurrence of free-fluid phases [e.g., *Nakajima et al.*, 2001; *Hacker et al.*, 2003a], pore geometry [e.g., *Takei*, 2002], reaction kinetics [*Evans*, 2004; *Perrillat et al.*, 2005], suitable mixing models used to convert velocity data in mineral composition [e.g., *Ji and Wang*, 1999], or medium to large-scale rock heterogeneity (lattice preferred orientations, compositional layering [*Ji and Wang*, 1999]).

[26] Contribution of metamorphic sediments and/or greywackes within the subducting upper crust, as proposed for the Wellington DSZ, New Zealand [*Zhang*, 2003], could drastically reduce Vp/Vs

ratios [*Christensen*, 1996]. However, such a hypothesis is unlikely in northern Chile because the subducting Nazca plate is known to have experienced very few pelagic deposits (<850 m [*Prince and Kulm*, 1975]). This feature is a direct consequence of the arid climate affecting the southwest intertropical coast of South America [e.g., *Lamb and Davis*, 2003, and references therein].

[27] Petrological diversity in mantle material is rather limited. Nevertheless, addition of magnetite and clinopyroxene (diopside + jadeite) tends to increase the Vs values of the partially hydrated harzbugitic material used in our simulations. Occurrence of magnetite is common in serpentinized rocks where it reaches up to 10 vol % of the rock [e.g., *Coleman and Keith*, 1971]. Significant amounts of clinopyroxene (>8 vol %) suggests that lherzolitic or wehrlitic layers could be interstratified within the harzburgitic material, a feature observed in some ophiolitic complexes that are considered to be typical of oceanic lithosphere (i.e., Oman ophiolites [*Ceuleneer et al.*, 1988; *Benn et al.*, 1988; *Takazawa et al.*, 2003]). This presence of clinopyroxene-rich layers in harzburgitic material brings up an another problem generally not considered in large-scale models [e.g., *Hacker et al.*, 2003a, 2003b; *Hacker and Abers*, 2004]: rock heterogeneity. The main characteristic of natural outcrops of mafic or ultramafic materials is their textural heterogeneity [e.g., *Ceuleneer et al.*, 1988; *Benn et al.*, 1988; *Clarke et al.*, 1997; *Carson et al.*, 1999; *Takazawa et al.*, 2003]. For example, jadeite-lawsonite blueschists and eclogites commonly exhibit metric, decametric or kilometric eclogitic, gabbroic lenses or layers, and peridotites generally contain pyroxenitic layers or dykes. In addition, some layers are more intensively deformed whereas others are less deformed (i.e., gabbroic or eclogitic lenses in blueschists, serpentinite layers in peridotites). Such features introduce significant anisotropy that could have important consequences on measured seismic velocities. In particular, it is remarkable that the northern Chile DSZ lower plane displays Vp velocity values indicative of partly serpentinized peridotite (7.4 km/s) but Vs velocity values typical of anhydrous peridotite (4.7 km/s). The possibility that these data represent a fully serpentinized matrix containing anhydrous harzburgite lenses or layers should be explored. Nevertheless, such a hypothetical concept needs to be experimentally tested.

[28] Many authors [e.g., *Nakajima et al.*, 2001; *Takei*, 2002; *Hacker et al.*, 2003a, 2003b] suggest that the presence of free $H_2O$-rich fluids phases can explain low Vp/Vs ratios. The occurrence of water in excess is certainly required by the modeling of amphibole-rich eclogitic rocks in the work by *Carson et al.* [1999]. Hydrous minerals, mainly chlorite, hornblende, epidote or lawsonite for mafic compositions, and antigorite, chrysotile, talc-like phase, or chlorite for ultramafic compositions are the source of the water released during prograde metamorphism. Discontinuous dehydration reactions and/or entrapment of water by physical processes during continuous dehydration could lead to the observed low Vp/Vs, and hence favor seismicity. Kinetics is an important factor that can affect the modeling. Petrogenetic grids are based on equilibrium thermodynamics. Yet, as the slab moves downward, rapid changes in P and T can lead to kinetics driving reactions. Experiments by *Perrillat et al.* [2005] suggest that antigorite could breakdown at temperatures much below equilibrium petrogenetic grids (e.g., 520°C at 4 GPa), thus consistent with release of water at low temperature, especially if fluid is taken out from the medium at the same rate as it is produced. *Jung et al.* [2004] have also shown that antigorite breakdown under shear stress does not follow equilibrium thermodynamics, and that dehydration embrittlement could be the process for continuous dehydration.

[29] Another parameter that can significantly affect the rock Vp/Vs ratios is the pore geometry [*Watanabe*, 1993; *Takei*, 2000, 2002]. For example, a specific pore configuration (i.e., tube geometry, equilibrium geometry [*Watanabe*, 1993]) corresponding to low hydration and water-undersaturated pores could be responsible for the observed velocities in the intermediate zone of the DSZ.

[30] All our previous petrological interpretations of seismic velocities are based on data provided by *Hacker et al.* [2003a] and *Hacker and Abers* [2004], for which oceanic lithosphere materials are assumed restricted to an average MORB composition for the crust and an average harzburgite composition for the mantle. In order to explain our measured seismic velocities, we had to assume very specific compositional characteristics, and especially very cold conditions. Obviously other parameters such as rock heterogeneity and fluid configurations still require additional investigations in order to accurately evaluate their relative contribution. Meanwhile, an attempt to provide additional constraints is made in the following section, first by presenting the thermal and geophysical characteristics of both the subducting and the

overriding plates, and then by developing thermo-mechanical models of the northern Chile subduction zone.

## 3. Thermomechanical Modeling

[31] The idea is to setup a model with "reasonable" initial thermal and rheological structure, close to the northern Chile conditions, and to record stress buildup and propagation of deformation when applying upper plate convergence and basal slab-pull, over a relatively short timescale of 2 Ma. We present first the available data on the thermal structure of the region (section 3.1), referring to surface heat flow measurements, existing thermal studies, and geophysical data. We then describe our numerical thermomechanical approach (section 3.2), which differs from standard thermal models of subduction zones. A reference model is then presented, illustrating the general dynamics of deformation, resulting from specific initial conditions. With this model, we discuss the pressure-temperature specificities for the northern Chile DSZ (section 3.3). Finally, we illustrate with alternate models how the oceanic and continental thermal structures, the subducting channel rheology, and relative plate convergence, all affect these pressure-temperature conditions (section 3.4).

### 3.1. Thermal Structure in Northern Chile Inferred From Data

[32] Considering existing thermal studies of the northern Chile subduction zone, we first recall the heat flow data, studied by *Springer and Forster* [1998], who combined existing values [e.g., *Hamza and Muñoz*, 1996] with boreholes data. The mean heat flow density along a W-E generalized lithospheric structure shows the following trends:

[33] 1. Within the oceanic Nazca plate low values of about 30 mW/m$^2$ occur in the region of the Peru-Chile country boundary: these are low compared to the 70 mW/m$^2$ deduced from a 50 Ma old plate cooling model. *Springer and Forster* [1998] explained this value by a probable faster cooling resulting from heat convection compared to pure heat conduction models.

[34] 2. A minimum heat flow density of about 20 mW/m$^2$ is observed in the Coastal Cordillera, which would reflect cooling in the continental crust as a result of the subduction of oceanic lithosphere. Values increase toward the fore-arc region to 40–60 mW/m$^2$.

[35] 3. Heat flow varies from about 50 to 180 mW/m$^2$ in the area of the magmatic arc (sparse and equivocal) and the Altiplano. This large variability is interpreted by *Springer and Forster* [1998] as heat sources resulting from isolated magma chambers at shallow depths (~10 km), in agreement with geological and geophysical information (see review by *Schilling et al.* [2006]).

[36] 4. High values of about 80 mW/m$^2$ are typical for the back-arc region of the Eastern Cordillera, attributed to either doubling of the crust or rise of the asthenosphere.

[37] 5. Heat flow density is about 40 mW/m$^2$ in the Subandean Ranges and Chaco Basin, somewhat lower than the 50–60 mW/m$^2$ of the adjacent Brazilian Shield farther to the east [*Hamza and Muñoz*, 1996].

[38] Geophysical investigations also give insight on the thermal structure of northern Chile. We summarize here a review by *Schilling et al.* [2006]. From magnetotelluric investigations, the volcanic arc does not appear as a conductive feature along the three MT profiles carried north of 21°S, but show instead a low-conductivity zone, and very low conductivity in the fore arc beneath the Coastal Cordillera, extending into the upper mantle [e.g., *Brasse et al.*, 2002]. However, there is a broad and intense anomaly in the midcrust beneath the plateau at least 40–50 km deep (note that this is more than 350 km east of the trench), with evidences for a conductive root reaching the upper mantle, possibly representing the mantle wedge [*Brasse*, 2005]. Seismic waves through the fore-arc crust indicate a cold crust containing only minor free fluids, and Qp tomography shows no indication of a fluid "curtain" extending from the descending slab into the fore-arc region. Some regions of the fore arc show extremely low attenuation, indicative of a strong, cold lithospheric block [e.g., *Haberland et al.*, 2003; *Schurr and Rietbrock*, 2004]. This may impede magma generation, and explain the observed shift of the volcanic arc to a depth to the top of the slab reaching 110–130 km (e.g., global study by *Syracuse and Abers* [2006]).

[39] The thermal structure of our numerical model should thus be constructed to comply with these data, and will be mostly based on previous thermal models developed by *Springer* [1999], and gravity models by *Tassara et al.* [2006]. This setup will be described in detail further in section 3.2.2, after having first presented our general numerical approach.

**Table 3.** Notations and Physical Values Common for All Experiments[a]

| Parameter | Values and Units | Definition |
|---|---|---|
| P | Pa, MPa | stress, pressure |
| $\varepsilon$ | s$^{-1}$ | strain |
| $\mu$* | $10^{10}$   $10^{20}$ Pa s | effective viscosity |
| $\phi$ | 1.43   20° | friction angle (see Table 4) |
| So | 10 MPa | cohesion |
| $\lambda$, G | 30 GPa | Lamé elastic constants ($\lambda$   G) |
| Vx | **3 cm/a   0** | horizontal upper plate convergence |
| Vb | 5 cm/a | basal slab pull velocity |
| r | **250   450 km** | radius of curvature of oceanic plate |
| hc | 35   55 km | normal and prethickened continental Moho depth |
| hl | **120   180 km** | thickness of lithosphere |
| T, To, Tb | 10   1350° | temperature, surface, base |
| Cp | 10 J/kg/°C | specific heat |
| $\Delta T$ | 9   12°C/km | initial arc anomaly, with maximum at X   330   530 km |
| $\alpha$ | $3 \times 10^{-5}$/°C | Thermal expansivity |
| kc | 2.5   2.9   3.3 W/m/°C | thermal conductivity, crust, mantle, channel |
| H | $9. \times 10^{-10}$ W kg$^{-1}$ | radiogenic heat production, constant |
| hr | 10 km | radiogenic heat production exponential decay depth |
| AC | 400 Ma | thermotectonic age of the continental lithosphere |
| AO | **60   150 Ma** | age of the oceanic lithopshere |
| lc | 10 km | thickness of subduction channel |
| ke | 25, 2000 m$^2$/a | erosional diffusion coefficient, left and right of the Eastern Cordillera |

[a] *Turcotte and Schubert* [1982]. Bold values are those that were tested and displayed in Figure 8.

## 3.2. Thermomechanical Modeling Approach

[40] We do not wish to account for full thermodynamical modeling of subduction processes in northern Chile, for various reasons:

[41] 1. This subduction zone has been ongoing for almost 80 million years with still debated alternances of extensional and compressional upper plate arc regimes. For example, the very characteristic Altiplano feature that has built on the upper plate obviously indicates specific deep structural properties, and its rise, linked with the formation of the Arica elbow, is still debated to have occurred since either within the last 10 Ma or 35 Ma ago [e.g., *Roperch et al.*, 2006, and references therein].

[42] 2. Full thermomechanical models have already been published by *Sobolev and Babeyko* [2005, 2006], over a time duration of about 20 Ma. Since in fact, a number of geophysical data and conceptual models of the present-day structure of the northern Chile margin exist, instead in this study, we wish to reproduce on a relatively short timescale of about 2 Ma, specific deformation and stress patterns surrounding the subduction zone interface. Therefore, we start from an hypothetical thermal structure, a geometrical structure and a rheological layering, that are built as close as we

can to available published information, and which, implicitly, assume a relative thermal steady state and dynamical equilibrium of the forces in play.

[43] We use a Lagrangian approach that simulates elastic-viscous-brittle behavior, Parovoz [*Poliakov and Podladchikov*, 1992], a 2-D finite differences numerical code based on the FLAC technique [*Cundall and Board*, 1988]. It resolves differential equations alternately, with the output for the solution of the equations of motion used as input to the constitutive equations for a progressive, time explicit, calculation. FLAC is based on a quadrilateral mesh formed by superimposing two constant stress/constant strain triangular finite elements. Each element behaves according to prescribed stress/strain constitutive laws in response to kinematical boundary conditions: Mohr-Coulomb nonassociative elastoplasticity is combined with temperature-dependent viscoelasticity (Maxwell) so that locally, the minimum of both stresses is chosen. Accounting for elastic-brittle-ductile properties permits to model formation of faults or shear zones and lithospheric extension and collision [e.g., *Poliakov et al.*, 1994; *Lavier et al.*, 1999; *Burov and Poliakov*, 2001; *Gerbault et al.*, 2003]. The free upper surface boundary allows to adequately resolve for surface processes, which are accounted for with a diffusion equation with variable coefficient (Table 3). The basic equations of
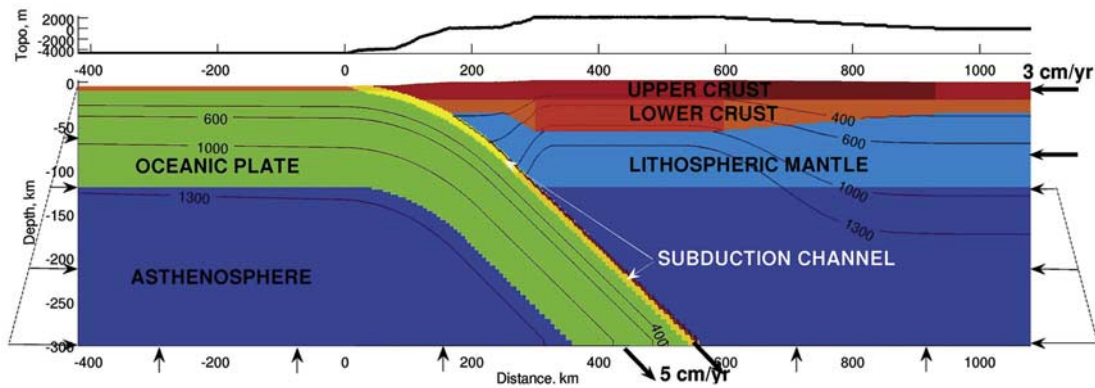
**Figure 5.** Initial conditions for the thermomechanical model: each colored layer has specific rheological density and thermal properties (see Tables 3–5). Isotherms 400, 600, 1000, and 1300°C are contoured. Asthenospheric and continental mantle are shown in blue, crustal layers are shown in red to brown, oceanic plate is shown in green (crust is in orange), and subducting channel is shown in yellow and light orange. Initial topography is evaluated from initial isostatic equilibrium. Boundary conditions are lithostatic compensation on the sides and at the base of the model (narrow black arrows), except at the base of the slab and along the right edge of the continental lithosphere, where velocities of 5 cm/a (slab-pull) and 3 cm/a (upper plate convergence), respectively, are applied (bold arrows).

motion and heat transport in Lagrangian formulation for Parovoz can be found in a number of publications [e.g., *Burov et al.*, 2003; *Gerbault et al.*, 2003; *Le Pourhiet et al.*, 2004; *Yamato et al.*, 2007]. The heat transport equation accounts for heat conduction, radioactive and shear heating, while heat advection is accounted for by the displacements of the Lagrangian grid. This version of Parovoz does not account for phases reactions and subsequent density evolution, and employs a remeshing technique using passive markers similar to *Yamato et al.* [2007]. See Appendix C for more details.

### 3.2.1. Rheologies and Boundary Conditions

[44] The model (Figure 5) simulates an area 300 km deep by 1800 km wide, comprising a flexuring oceanic plate dipping at 35°. With 900 × 150 grid elements, horizontal resolution is 2 km, and vertical resolution decreases downward from 1 to 4 km. Geometrical, rheological and thermal properties are summarized in Tables 3–5. Elastic, brittle and power law creep parameters are chosen according to various sources from rock mechanics extrapolated to the lithospheric scale [e.g., *Kirby et al.*, 1996; *Ranalli*, 1995, and references therein], and combined with the known special conditions for the Andes [e.g., *Springer*, 1999; *Tassara*, 2005; *Sobolev and Babeyko*, 2005]. Composition and densities are defined mostly according to the recent three-dimensional density model from *Tassara et al.* [2006], who compiled appropriate characteristics of the Chilean Andes.

[45] The following heterogeneities are inserted (see Tables 4 and 5). First, in the continental crust (various red to brown colors in Figure 5): the upper

**Table 4.** Model Parameters: Density ($\rho$), Compared to Those Chosen by *Tassara et al.* [2006], Dominant Composition (Labels Given in Table 5), Friction ($\phi$), and Conductivity (k) for Model Layers[a]

| | Oceanic Mantle | Oceanic Crust | Asthenosphere | Continental Upper Crust | Continental Lower Crust | Continental Mantle | Subducting Sediments | Subduction Channel |
|---|---|---|---|---|---|---|---|---|
| $\rho$ | 3350 | 3050 | 3350 | 2750 | 3050 | 3340 | 2750 | 3250  3370 |
| $\rho_{Tassara}$ | 3260  3500 | 2980 | 3310  3450 | 2700 | 3100 | 3240  3320 | 2980 | 2980  3550 |
| Composition | *oldry* | *mfgr* | *oldry* | *qz* | *mfgr* | *olwet* | *plg* | ***wetgr plg*** |
| k | 3.3 | 2.9 | 3.3 | 2.5 | 2.5 | 3.3 | 2.9 | 2.9 |
| $\phi$ | 20° | 15° | 5° | 15° | 15° | 5° | 5° | 1.5° |

[a] Value in bold was modified for the model in Figure 9d.

**Table 5.** Dislocation Creep Parameters, After References Provided by *Ranalli* [1995][a]

| | Dry Olivine *oldry* | Wet Olivine *olwet* | Mafic Granulite *mfgr* | Plagioclase *Plg* | Quartz *qz* | Wet Granite *wetgr* |
|---|---|---|---|---|---|---|
| $n$ | 3 | 2.5 | 4.2 | 3.2 | 2 | 1.9 |
| $A$ (MPa$^{-n/s}$) | 7.e4 | 3.e4 | 1.4e4 | 3.3e 4 | 1.e 3 | 2.e 4 |
| $Q$ (J mol$^{-1}$) | 5.2e5 | 4.44e5 | 4.45e5 | 2.38e5 | 1.67e5 | 1.37e5 |

[a] $n$, power exponent; $A$, material constant; $Q$, activation energy.

crust is supposed to be of weak composition in the Bolivian foreland [e.g., *Sobolev and Babeyko*, 2005], as opposed to the fore-arc crust, which is of rather mafic composition, coherent with geophysical data and geological history (e.g., flexural rigidity study by *Tassara* [2005, 2006], seismology and magnetotellurics reviewed for example by *Schilling et al.* [2006], and geology indicating long-lived arc magmatism [*Lucassen et al.*, 2001]). The Altiplano domain is characterized by a prethickened lower crust (65 km with respect to 35 km elsewhere), which has a more felsic behavior [e.g., *Lucassen et al.*, 2001; *Beck and Zandt*, 2002].

[46] Second, the subduction channel, defined 10 km thick, is composed of three portions: the upper 10 km mimic unconsolidated oceanic crust, with a plagioclase rheology and a moderate friction angle of 5°. Below, weaker wet granite rheology is employed (this choice is discussed later on) and friction is 0.025 (angle of 1.43°), corresponding to the mean value proposed by *Lamb* [2006]. At 120 km the density of the channel increases, mimicking eclogitization.

[47] The driving boundary conditions are (1) a westward velocity Vr = 3 cm/a applied from the eastern edge of the model lithosphere, simulating South America plate motion, and (2) a velocity traction Vb = 5 cm/a inclined at 35°downward exactly where the oceanic plate intersects the base of the model at 300 km depth (similar to *Sobolev and Babeyko* [2005]). Lithostatic normal stresses are applied at the base and lateral borders of the model at asthenospheric depths, and along the extremity of the oceanic plate along the left border.

[48] Mechanically, we start from a geometrical configuration of layers of different density, which are compensated only in the vertical direction with the appropriate initial topography. About 1 million years are needed for the model to build up stresses and deform internally in response to applied asymmetric slab-pull and upper plate driving forces. This timescale is defined by elastic and yield

parameters and the loading strain rate, and can be roughly estimated from 1-D Hooke's law: with a maximum yield stress close to 1 GPa, a standard Young's modulus equal to 30 GPa, and ~7 cm/a of horizontal compression applied over a model length of 1800 km.

### 3.2.2. Thermal Structure

[49] Thermally, we proceed similarly as in the mechanical approach, in the sense that we presume of initial temperatures close to steady state, that will not evolve significantly during the 2 Ma of the model duration: heat conduction, radioactive heating and shear heating, as well as convective heat transport are all directly limited by the short duration of the run. This short 2 Ma timescale also allows us to neglect evolving phase transformations (eclogitization or serpentinization of the oceanic crust), partial melting, or thermochemical effects. The initial thermal structure is thus based on previous estimates by *Springer* [1999] and *Tassara et al.* [2006]. We first calculate oceanic and continental geotherms as a function of their thermal age [*Parsons and Sclater*, 1977; *Turcotte and Schubert*, 1982; *Burov and Diament*, 1995]. We choose an age of 60 Ma for the oceanic lithosphere, in order to deal with a lithosphere, only slightly but reasonably colder than the unsatisfying "theoretical" 50-Ma-old age. We thus have surface values of 60 mW/m², still greater than the measured 30–40 mW/m². Implications will be discussed later on. For continental temperatures, we define the thermal depth of the continental plate at 180 km [*Tassara et al.*, 2006], standard radiogenic crustal heating (see Table 3), and insert a Gaussian shape thermal anomaly initiating from the interplate contact, extending below the Altiplano thickened crust to the Subandean area, that superimposes on *Tassara et al.* [2006] estimation of the lithosphere-asthenosphere boundary. *Tassara et al.* [2006] obtained a lithosphere-asthenosphere boundary (isotherm 1350°C) moving up to 60 km depth below the Western Cordillera and Altiplano, descending down to 160–180 km depth further

east (Figure 5). At the interplate contact, *Springer* [1999] used a heating shear stress of 15 Mpa, whereas *Lamb* [2006] employs 10 MPa, from seismic coupling arguments: we insert an interface shear heating stress of 10 MPa.

[50] In fact, we will not follow here the standard approach for thermal modeling of subduction zones, in which a kinematically prescribed slab drives a dynamic corner flow in the wedge under a stationary overriding plate [e.g., *Peacock and Wang*, 1999; *van Keken et al.*, 2002; *Kelemen et al.*, 2003; *Conder*, 2005; *Kneller et al.*, 2005, 2007; *Abers et al.*, 2006]. These thermal models use an Eulerian method that resolves the temperature equation for a steady state that is reached over several tens of millions of years (ideally 100 Ma), and allows to study the thermal influence of viscous mantle corner flow on the surrounding plates. Our approach here differs since we only aim at reproducing 2 Ma of thermomechanical dynamics, and therefore assume that the thermal state at the onset of the run is equivalent (e.g., does not change significantly) to that at the end of the run: this is a simplified hypothesis, that limits the development of significant mantle corner flow. We will discuss this limitation later on in the light of our results. On the other hand, the advantage of our approach compared to standard thermal models of mantle wedge corner flow, is that we do not fix the position or motion of plates in the subduction zone area during the run, thus we do not need to define special wedge boundary conditions [e.g., *Conder*, 2005; *van Keken et al.*, 2002], such as a progressive transition between the fixed part and the subducting part of the oceanic plate. Here in our models, no condition other than the initial temperature is applied, since the 10 km thick channel interface, like all other layers, is self-consistently defined with a temperature-dependent brittle-ductile behavior, located in between both deformable oceanic and continental plates. The approach is thus resolutely different.

### 3.2.3. Mechanical Behavior of the Reference Model

[51] Elements of the model progressively load and deform as they are submitted to the gravity force and the kinematic boundary conditions. They reach a stress threshold that depends on their rheological properties: warm zones deform ductilely, while cold zones deform brittly. We will here mainly describe deep stresses and temperatures in order to connect them with pressure-temperature (PT) petrological inferences from our tomography data. Stress and strain patterns in the continental crust will be only briefly described here, as it is not the aim of this paper to discuss this part of the modeling study, but will be done in another paper.

[52] 1. In the oceanic lithosphere (green domain in Figures 5 and 6c), flexural stresses develop because of its bended geometry. Before the trench at X ∼ 50 km, brittle shear zones develop at the surface, extending down to several tens of kilometers into the oceanic mantle (Figure 6b). These outer rise faults are compatible with previous observations of deep outer rise events along the Chilean margin [*Clouard et al.*, 2007]. As the oceanic lithosphere dips under the continent, tensile stresses develop in direction parallel to the applied slab-pull velocity (Figure 6e), together with high compressional stress on the top portion of the slab down to about 130 km depth (commented in section 3.3).

[53] 2. In the subduction channel (yellow to light orange zones in Figures 5 and 6c), shear deformation develops, at relatively low shear stress (Figure 6d). At the surface a trench forms about 8 km deep. The shear stress reaches ∼40 MPa down to ∼60 km depth (Figure 7a), consistent with previous estimates [e.g., *Lamb*, 2006, and references therein], and corresponds approximately to a brittle-ductile transition. Above, deformation occurs dominantly by brittle failure according to the Mohr-Coulomb criterion at constant friction angle (1.43), and corresponding to the seismogenic zone. Below 80 km depth, the subduction channel behaves ductile with a low effective viscosity ($<10^{20}$ Pa/s, Figure 7b).

[54] 3. The continental upper crust (brown, Figures 5 and 6c) deforms mostly brittle, and is partly ductile at ∼10 km depth in the Bolivian area (X > ∼550 km, Figure 6b). The lower crust (red, Figure 6c) remains competent and deforms little in the fore arc and in the cratonic easternmost domain, in contrast to the Altiplano, where weaker rheology and warmer temperatures enable to develop ductile shear deformation. This area below the plateau links deformation from the subducting slab, eastward to the surface in the eastern Bolivian weak upper crust [e.g., *Sobolev and Babeyko*, 2005]. This mode of simple shear deformation is consistent with previous propositions such as by *Tassara* [2005] and *Tassara et al.* [2007].
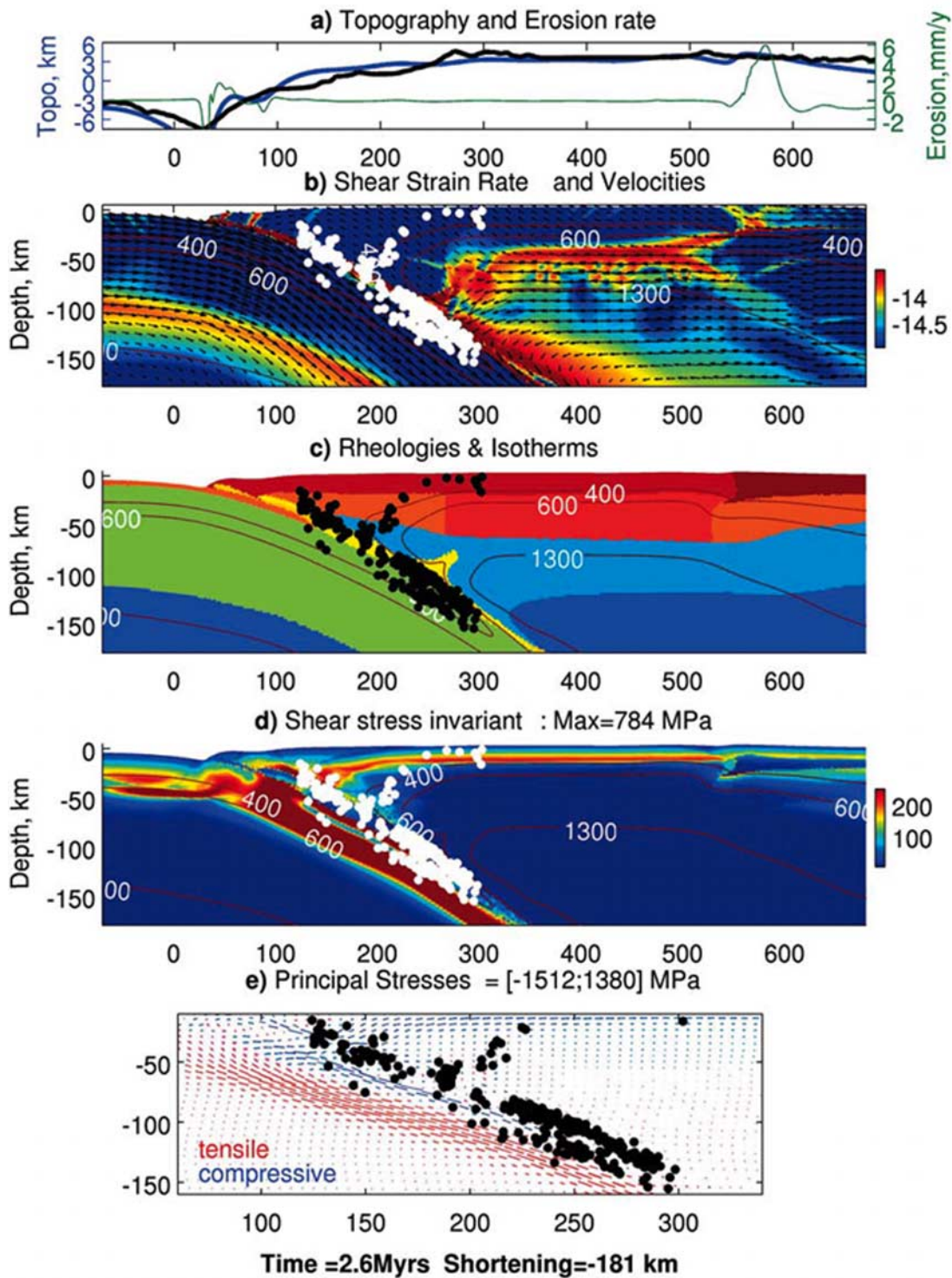
**Figure 6.** Reference model, with superimposed seismicity. (a) Modeled topography in blue, erosion rate in green, and real topography at 18.5°S in black. (b) Shear strain rate and velocity vectors, indicating in red areas of greater shear deformation, either brittle or ductile (note the outer rises). (c) Rheological layers and isotherms: note the 400°C isotherm. (d) Deviatoric shear stress indicating in red areas of stress greater than 250 MPa, in the slab and in the crust. Note some stress in the deep portions of the fore arc. (e) Crosses of the principal stresses, zoomed at the subduction zone, showing downdip compression above downdip tension and rotating and complex stresses in the fore arc.
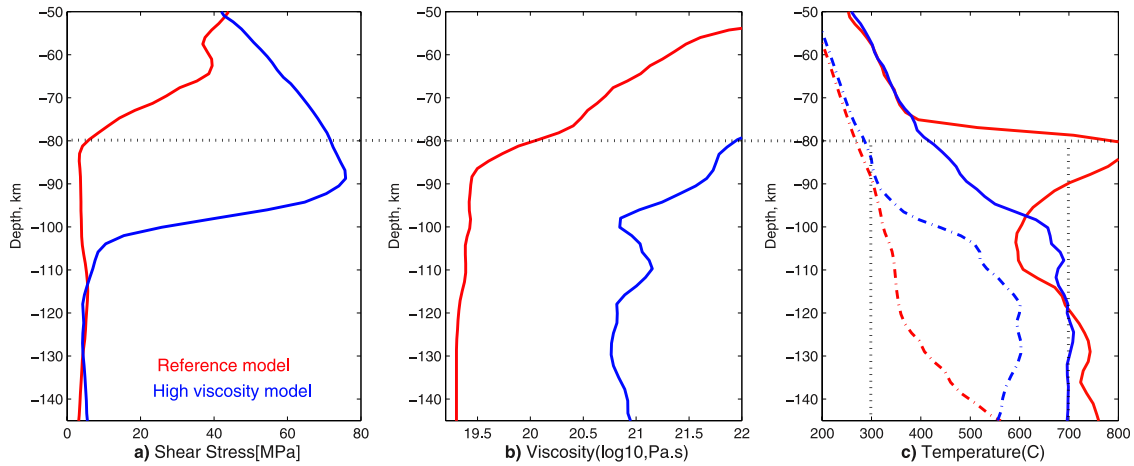
**Figure 7.** Thermomechanical properties of the subduction channel for reference model (red) and model with prescribed higher viscosity in the subduction channel (blue, Figure 9d). (a) Deviatoric shear stress, indicating for the reference model a maximum at ~50 km depth of 40 MPa, reducing to nearly 0 below ~80 km depth. (b) Effective viscosity, which becomes lower than $10^{20}$ Pa/s in the reference model, to the difference of the high-viscosity model. (c) Minimum (dashed lines) and maximum (plain lines) temperatures. Note that the great increase around ~85 km depth corresponds to the detachment and elevation of light oceanic crust material throughout the continental mantle (see yellow bubble in Figure 6c).

[55] 4. As a whole, the fore-arc area behaves as a rigid lithospheric-scale wedge, bounded to the east by the Western Cordillera, and extending down to ~110 km depth. This rigid block is cold and composed of strong crust and mantle rheologies, therefore deforms little (Figure 6b) [e.g., *Tassara et al.*, 2007]. Observed seismicity occurs in the range <400°C for crustal domains and <600°C for mantle domains (Figure 6c). However, stresses are not homogeneous (Figures 6d and 6e): seismicity occurs first at the high stress contact of the crust with the subduction channel, and then further east in slightly lower deviatoric stress areas. Principal stresses orientations indicate that this seismicity occurs in a downdip tensional zone at 30–80 km depth (red crosses at X = 140–230 km), and where the most compressive stress (blue crosses) rotates from horizontal to vertical at 10–40 km depth (X ~ 220–300 km).

[56] 5. The continental mantle (blue, Figures 5 and 6c) deforms little at temperatures lower than ~600°C, while it deforms ductile at greater temperatures, and with negligible shear stress (power law temperature dependant olivine rheology). East of and along the subduction channel below the fore arc, cold temperatures induce significant shear stress (around 100 MPa, Figure 6d) in the lithospheric mantle down to about 100 km depth. This cold "rigid mantle wedge" [e.g., *Honda*, 1985], or more recently named the cold nose [*Abers et al.*,

2006] is delimited on top by the base of the fore-arc crust, at its base by the warmer and ductile corner wedge, and to the west by the nearly vertical ~600°C olivine brittle-ductile transition. While recent thermal studies show the high capacity of mantle corner flow in heating the adjacent slab and the overriding plate [e.g., *Billen and Gurnis*, 2001; *van Keken et al.*, 2002; *Currie and Hyndman*, 2006; *Kelemen et al.*, 2003], coherent with heat flow and geophysical characteristics of several subduction zones, other thermal models also show that the development of a cold fore-arc mantle wedge is favored when the oceanic plate is old and subducts fast, and when a strong coupling is accounted for in between the fixed and descending parts of the oceanic plate [e.g., *Kneller et al.*, 2005; *Abers et al.*, 2006]. The data from northern Chile indicate such characteristics, with *Springer*'s [1999] thermal model indicating a shallowest depth of the asthenospheric wedge located 70 km below the Western Cordillera, and vertically descending isotherms down to about 100 km depth before intersecting with the slab (such verticalization is also assumed by *Abers et al.* [2006], for Cascadia). This cold fore-arc mantle remains the strongest layer of the continental lithosphere, and acts as a buttress to subduction, thus controlling deformation of the upper plate. It transmits compressional stresses from the upper plate, that apply perpendicular to the subduction zone, into the slab. The stresses that we obtain are in the range of those

cited by *Kneller et al.* [2005, 2007], who explain trench-parallel fast shear wave splitting directions by the presence of B-type olivine fabric in the fore-arc mantle. Heading east below the high plateau, high temperatures (1350°C at ~60 km depth) provide a low-viscosity behavior that may be associated with active mantle corner flow, coherent with magnetotelluric and seismological data. Below the Eastern Cordillera (X ~ 500 km) and eastward, progressive cooling recomposes a rigid, cratonic like behavior down to >150 km depth.

## 3.3. DSZ Pressure-Temperature Conditions Inferred From the Thermomechanical Model

[57] We display now the modeled pressure-temperature (PT) conditions in the double seismic zone, spread between 80 and 140 km depth along the slab. Figure 7 displays the thermal and stress conditions within the subducting channel crust, and Figure 8 shows pressure-temperature conditions within the slab. We superimpose the earthquake locations and the model (Figure 6) by assuming that at least the top part of the upper plane of earthquakes should be located inside the subducting oceanic crust channel (yellow in Figure 5). The uncertainty in this "visual" fit is about 5 km, because of the projection of seismic profiles on the curved in plane geometry of the trench at these latitudes, and to the thermomechanical grid size. Whereas it is common to assume that Wadati-Benioff earthquakes delineate the subduction channel, an uncertainty remains on this assumption, see for example a depth-dependent increasing decay in the work by *Abers et al.* [2006], for the Cascades subduction zone. However, note that in this latter study, this correspondence is preserved in the upper part of the Wadati-Benioff zone.

### 3.3.1. Upper DSZ Plane

[58] Figure 7c plots minimal and maximal temperatures within the subduction channel: whereas maximum temperatures reach 700°C at the top of the subducting crust, they can drastically decrease to about 300°C at the bottom base of the subducting crust, which in the model was defined 10 km thick. In between 90 and 130 km depth, minimum temperatures are ~100°C lower than those estimated by *Abers et al.* [2006] for the, yet shallower, seismic portion of central Cascadia subduction zone, where a younger 38 Ma oceanic lithosphere converges at a speed of 55 mm/a. Maximum temperatures, however are close to 700°C, which

is about 100°C less than what *van Keken et al.* [2002] obtained for the top of the Honshu slab below the volcanic arc. Considering the equivalent surface heat flow between both subducting plates in Honshu and northern Chile, we evaluate that this 100°C difference is linked with the obviously warmer general temperatures of the Honshu upper plate with respect to northern Chile (see previous sections).

[59] We have here a possible explanation for the distance measured by *Abers et al.* [2006] in Cascadia, between the earthquakes of the Wadati-Benioff zone and the low seismic velocity zone: the latter could represent the warmest and thus ductile top of the crust, whereas the former could represent the coldest and thus seismically active base of the subducting crust.

[60] In our prior estimates of petrological compositions using *Hacker and Abers* [2004] procedure, Vp and Vs values of northern Chile DSZ upper plane were best modeled with water-rich (up to 5.7 wt % $H_2O$), and mineral assemblages comprising omphacite, lawsonite, amphibole and chlorite (section 2.2.3). Thermodynamically calculated mineral equilibria for metabasaltic compositions [e.g., *Guiraud et al.*, 1990; *Clarke et al.*, 1997; *Carson et al.*, 1999] all indicate that such mineral assemblages only occur at temperatures below 570°C and are typical of blueschist conditions. In addition, the probable persistence of lawsonite in mineral assemblages suggests that temperatures, even at 3.5 GPa (~140 km) do not exceed ~700°C, the temperature at which lawsonite is no longer stable. Thus, independent mineralogical data are consistent with the low-temperature conditions of our thermomechanically modeled crust. Then, a fluid release associated with progressive breakdown of $H_2O$-rich phases, such as chlorite and amphibole, appears as the most probable scenario to explain this upper plane seismicity.

### 3.3.2. Intermediate Zone

[61] Our previous petrological estimates for this zone was a partially hydrated harzburgitic oceanic mantle, with however, remaining high Vp values with respect to Vs and Vp/Vs values (section 2.2.4). We note from the present thermomechanical models that along the subduction zone, the DSZ seismicity contours and bounds the shape of the inner slab compressive zone (Figures 6 and 8a) from 80 to 130 km depth. The intermediate zone is thus in a compressional state of stress, at approximately at least 400 MPa above lithostatic stress.
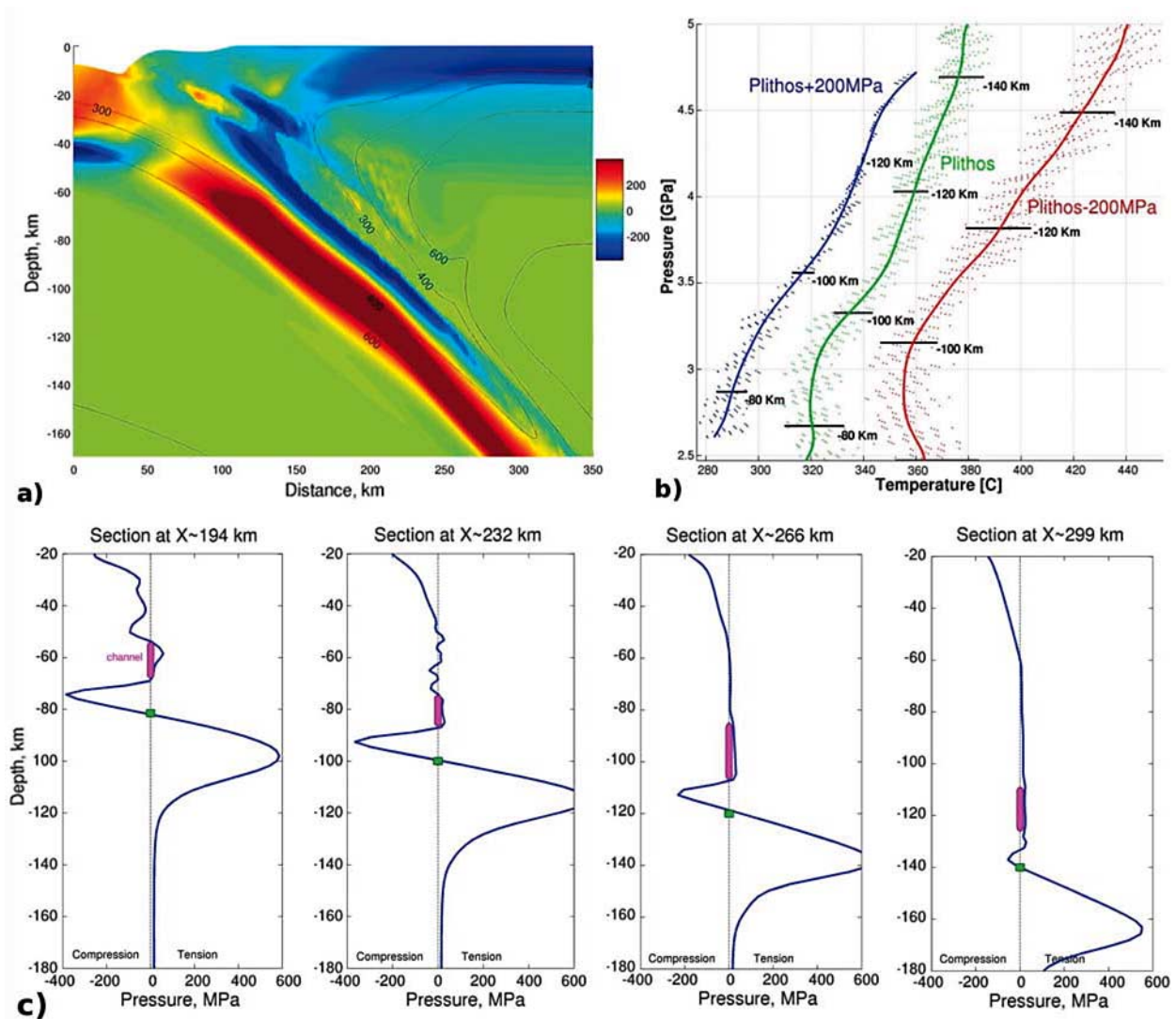
**Figure 8.** Pressure-temperature conditions obtained for the suggested lower seismic plane, located at the depth of the neutral plane in the subducting slab: (a) Background colors show pressure, with subtraction of the lithostatic component (compression is negative and blue). (b) Pressure-temperature paths: green markers (dots) and green line (mean value) show the neutral plane within the slab (labeled Plithos), indicating temperatures of 320–380°C at lithostatic pressure of 2.5–5 GPa. Pressure and temperature paths are also shown in blue and red for areas above and below this neutral plane, which are at an overpressure and underpressure of 200 Mpa, respectively, corresponding to the compressive stress (labeled Plithos + 200 MPa) and tensile stress (Plithos − 200 MPa) of Figure 8a. See Appendix C for numerical sampling details. (c) Vertical sections of pressure (tension > 0 here, and the lithostatic component is subtracted) throughout the fore arc, locating from left to right the neutral plane at depths 80, 100, 120, and 140 km (green squares). Note the ~15 km distance of this neutral plane with the subducting channel crust above, whereas the distance between maximum compression and maximum tension is greater than 25 km. Note the variable stress state, including tension, in the fore-arc mantle and in the channel area (pink ellipses).

Such overlithostatic pressures of several hundreds of MPa tend to increase Vp [*Hacker et al.*, 2003a], thus offering an explanation to the relative high numbers measured in northern Chile. We may therefore evaluate that this intermediate zone is even less hydrated than previously estimated.

### 3.3.3. Lower DSZ Plane

[62] If the upper plane's seismicity represents indeed the subducting oceanic crust, then the observed lower plane's seismicity falls in the model, on the neutral plane of the subducting mantle located about 20 km below the top of the slab (Figures 8a and 8c). There, pressure becomes

lithostatic as it switches from downdip compression to downdip tension (Figures 6e and 8c). This neutral plane could form a secondary channel of "relaxed" pressure, into which fluids from lateral areas could migrate: tensile stresses below the neutral plane should help open pores and let light fluids migrate upward, whereas compressional stresses above the neutral plane should close pores and create a permeability barrier to fluid ascent. Consequently, free fluids could remain trapped in this neutral plane. Earthquakes may thus be triggered close to and on either side of this neutral plane, because of the presence of free fluids. Within a partially hydrated harzburgitic material (the most probable candidate deduced in section 2.2.5), such a free-fluid phase pore configuration could explain the observed low Vp/Vs ratios, as suggested by many authors [e.g., *Nakajima et al.*, 2001; *Takei*, 2002; *Hacker et al.*, 2003a].

[63] Seismic events occurring in this lower DSZ plane should therefore not present any dominant compressional or extensional focal mechanism, but will rather occur depending on their position either slightly above or slightly below this neutral fiber. In fact, previous studies worldwide cannot isolate a common trend for the location of compressional or extensional events in the upper and lower plane of DSZs respectively, nor the opposite (cf. review by *Peacock* [2001]). Our proposition here differs from previous studies that link upper and lower seismic planes to high deviatoric stresses in the downgoing crust and mantle [e.g., *Wang*, 2002], and for which the elastic core is located in between both seismic planes. Here instead, we propose that the plate's stress neutral fiber has not kept a significantly thick elastic core [e.g., *Sleep*, 1979], but consists of an already fractured area (such as by outer rise faulting) in which fluids have accumulated and trigger neighboring seismogenic dehydration reactions.

[64] Note that in Figure 8c, the minimal distance between the subducting channel and the neutral lithostatic stress is closer to 15 km than to 20 km. We think that this is due to our choice of a relatively warm subducting oceanic lithosphere (60 Ma old) with respect to real conditions inferred from surface heat flow values (corresponding to classical 100 Ma old oceanic lithospheres). With a colder lithosphere, this distance increases, as indicated by *Brudzinski et al.*'s [2007] study and an alternate cold model (section 3.4). Furthermore, if instead we try to associate the upper and lower plane seismicity to the compressional and extensional zones of the subducting lithosphere respec-

tively, then we see that their distance in the model is 25 km (Figure 8c), which is not satisfying either, and will even increase if a colder oceanic lithosphere was assumed.

[65] In general, our modeled temperatures are about 100°C lower than those predicted for the Honshu lower seismic plane. Petrological interpretations indicate conditions lower than about 500–600°C, while our thermomechanical models indicate conditions around 400°C. There are several possible explanations:

[66] 1. Temperatures in the northern Chile subduction zone are anomalously cold: first the Nazca plate has anomalously low surface heat flow (30 mW/m$^2$ instead of the theoretical 70 mW/m$^2$ [e.g., *Springer and Forster*, 1998]), then the overriding plate presents geophysical characteristics of a rigid cold fore arc as opposed to a very weak and warm Altiplano, indicative of an eastward shift of the warming mantle wedge corner flow [e.g., *Haberland et al.*, 2003; *Brasse*, 2005]. *Honda* [1985] had already suggested that the mantle fore arc of central South America is probably cooler than that of the Honshu region, possibly associated with the different nature of volcanic rocks in both regions. More recently, *Kneller et al.* [2007] proposed to explain trench-parallel fast shear wave splitting directions in the fore-arc mantle of several subduction zones, including northern Chile, by the presence of B-type olivine fabric, associated with a relatively cold and a high-stress environment. Since we used in our models a Nazca plate age of 60 Ma giving surface heat flow values of 60 mW/m$^2$, we may still be overestimating inner slab real temperatures.

[67] 2. The numerical models carried here have assumed simple thermal properties that are basically diffusing and advecting during a short 2 Ma time: there is no account for thermal expansion, nor for latent heat linked to phase transformations. Certainly the long-lived subduction zone of Chile incorporates greater complexity than the present models do. Several studies showed that power law viscous flow in the mantle wedge is capable of heating the plate interface temperatures by about 200°C compared to isoviscous cases [e.g., *van Keken et al.*, 2002; *Conder*, 2005]. Although here we use a similar power law rheology, the short duration of the model (2 Ma) limits the efficiency of convective heat transport. We may thus be underestimating slab interface temperatures. However, *van Keken et al.* [2002] also showed that thermal gradients toward the inner core of the slab may

remain high, especially in cases of fast subduction of cold lithosphere, thus preserving its initial cold state to great depths. Consequently, we may be underestimating temperatures at the top of the slab, but not that much inner slab temperatures.

## 3.4. Testing Various Parameters

[68] The reference model of Figure 6 is our preferred model with which we discussed the PT conditions for the DSZ of northern Chile. But in order to obtain these appropriate PT conditions, we had to tune a number of initial parameters. Figure 9 shows a set of five alternate models, which illustrate the effect of varying some parameters with respect to the reference model (Figure 9a and Table 6):

[69] 1. First, if we take a 100 Ma old subducting oceanic plate (Figure 9b), then the modeled surface heat flow better matches the data from northern Chile. The 400°C isotherm and the compressional domain on top of the slab extend deeper down to about 180 km, in good correlation with the deeper DSZ of Honshu (plate age of 130 Ma). Our petrological interpretations, which strongly suggest a cold oceanic plate, still agree with this thermal setting.

[70] 2. Second, if we take warmer conditions in the overriding plate (Figure 9c), the intensity of the compressional zone vanishes. In this model, the continental thermal thickness ($hl$) was decreased to 120 km, and the thermal anomaly was increased. There, the warm fore-arc mantle flows ductilely and cannot transmit that much high stresses from the upper plate into the subducting plate. Other lines of evidence indicate that the fore-arc mantle in northern Chile is competent, such as thermal studies and gravity modeling [e.g., *Honda*, 1985; *Tassara et al.*, 2007]. Also, it must be competent enough in order to sustain the stresses generated by the extremely thick crust of the central Andes. In the opposite case, the Altiplano would collapse and present-day deformation would concentrate within the fore-arc and high-plateau areas, and this is not observed. Deformation now mainly occurs in the Bolivian foreland.

[71] 3. Third, the composition of the subduction channel (Figure 9d) was modified with ductile creep parameters corresponding to plagioclase, replacing wet granite in the reference model. Now, viscosities are greater in the subduction channel, and higher shear stresses develop there (comparison with the reference model in Figure 7). Shear stresses in the subducting channel below about 80 km depth, absorb part of the normal

(and thus compressional) stresses acting on one side and the other of the subduction zone, thus reducing the compressional component that is transmitted from the upper plate into the slab.

[72] 4. Fourth, the radius of curvature of the subduction zone was reduced to 250 km instead of 450 km (Figure 9e). The radius of curvature, $r$, estimated from Wadati-Benioff zones, mostly ranges from 200 to 500 km [e.g., *Wang*, 2002]. While Honshu and Chile have a similar radius of 450–500 km, New Zealand's dipping seismic zone approximates a 300 km arc radius [*Reyners et al.*, 2006]. In this model, compression on top of the slab extend to a shallower depth, consistent with shallowing of the plates unbending depth, but is also extends to greater depth, indicating that plate unbending there, has no more role to play. The slab is seen here to act like a vertical wall that "buttresses" horizontal compression.

[73] 5. Fifth, no upper plate convergence was applied (Figure 9f), the right boundary of the model was maintained fixed in the horizontal direction. In addition, the overthickened crust of the Altiplano was removed, in order to inhibit the local lateral compression exerted by gravitational forces. Now, the intensity of compression on top of the slab is much lower, showing that upper plate convergence is indeed important in the development of inner slab compression.

[74] These alternate models demonstrate that the inner slab flexural compressional zone does not only depend on the subducting plate age, but also on the regional stress environment. Transmission of compressional stresses from the upper plate into the subducting plate in turn, depends on lubrication of the subducting channel, thermal and rheological states of the overriding plate, and relative plate convergence.

## 4. Conclusion

[75] The results of a high-resolution tomography of the Nazca plate double seismic zone beneath north Chile, combined with a thermomechanical numerical modeling of the subduction zone, provides new insights on the petrological and thermodynamical properties of the oceanic plate and overriding continental fore arc. The velocity structure of the upper 140 km of the slab has been obtained, taking advantage of the two seismic planes observed at depths 80 to 140 km. The results highlight the specific characteristics of the zones where earthquakes occur. Moreover, the geodynamical
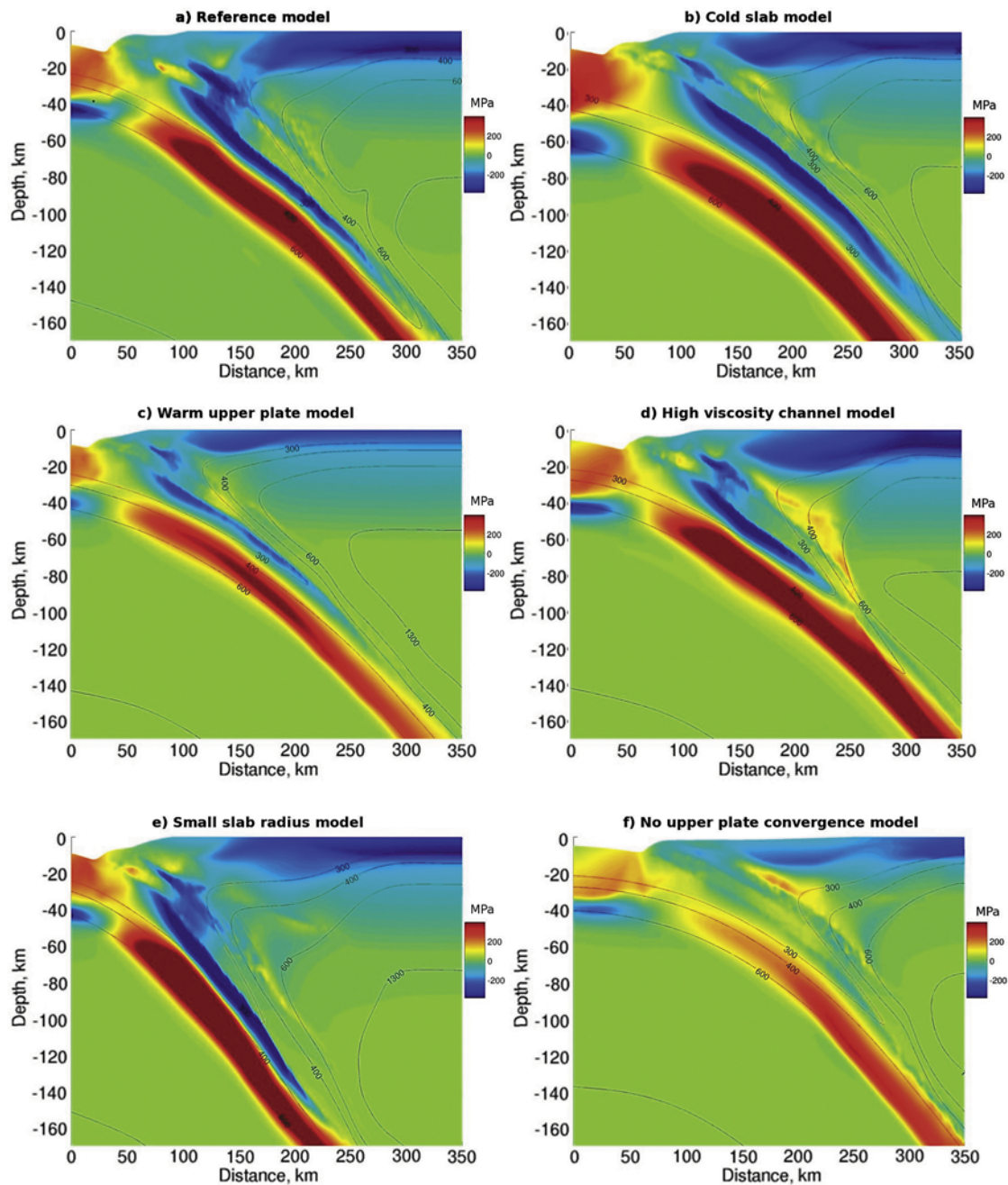
**Figure 9.** Reference model and five alternate models, showing pressure (the opposite of compression which is negative here, in blue) minus the lithostatic component, and isotherms along the slab. (a) Reference model. (b) Cold 150 Ma old oceanic plate. The 300°C isotherm exceeds 160 km depth and inner slab compression is high, broadens, and deepens. (c) Warm continent. The 400°C isotherm narrows and compression shallows to 100 km depth. (d) High viscosity of the deep subduction channel. Tension propagates into the fore arc and inner slab compression vanishes at 90 km depth. (e) Small slab curvature of 250 km. Isotherms deepen and inner slab compression elongates from ~30 to 160 km depth. (f) No applied upper plate convergence and no prethickened crust. Blurry compression appears from 80 to 120 km depth.

**Table 6.** Models' Tested Parameters[a]

| | Oceanic Plate Age | | Continental Temperature | Creep Parameters for Channel | Plate Curvature | Upper Plate |
|---|---|---|---|---|---|---|
| Reference model | **60 Ma** | *hl* | **180 km + 9°/km** | **wet granite** | **450 km** | **3 cm/a + prethickened crust** |
| Old oceanic plate | **160 Ma** | *hl* | 180 km + 9°/km | wet granite | 450 km | 3 cm/a + prethickened crust |
| Warm continent | 60 Ma | *hl* | **120 km + 10°/km** | wet granite | 450 km | 3 cm/a + prethickened crust |
| High viscosity channel | 60 Ma | *hl* | 180 km + 9°/km | **plagioclase** | 450 km | 3 cm/a + prethickened crust |
| Small plate curvature | 60 Ma | *hl* | 180 km + 9°/km | wet granite | **250 km** | 3 cm/a + prethickened crust |
| No upper plate compression | 60 Ma | *hl* | 180 km + 9°/km | wet granite | 450 km | **0 cm/a** |

[a] Specific variation for each model is shown in bold (see Figure 9).

setting leading to the observation of the DSZ, as well as its pressure and temperature conditions have been investigated by the thermomechanical modeling. A summary follows:

[76] 1. The DSZ in northern Chile is observed between 80 to 140 km depth. Both seismic planes are separated by ∼20 km.

[77] 2. The upper seismic plane, corresponding to oceanic crust, is characterized by intermediate Vp (∼7.7 km/s) and low Vp/Vs (1.67). These values suggest that between 80 and 140 km depth, the seismic upper plane is related to fluids releases associated with metamorphic reactions occurring within jadeite-lawsonite blueschists and perhaps, at higher depths (∼130 km) under lawsonite-amphibole eclogite conditions.

[78] 3. Seismicity in the lower plane, lying in the oceanic mantle, yields low Vp (∼7.4 km/s) and low Vp/Vs (∼1.57). These values are consistent with the common hypothesis of seismic activity associated with water release resulting from brucite, chlorite and antigorite breakdown in dehydration reactions occurring within serpentinized harzburgite (antigorite ≤ 25 vol %).

[79] 4. The region in between the two planes, with high Vp (8.5 km/s) and high Vp/Vs (1.9), presents characteristics corresponding to a moderately serpentinized harzburgite (antigorite ≤ 10 vol %).

[80] 5. Our petrological estimates infer general thermal conditions lower than 600°C. This low temperature range in comparison to estimates from other subduction zones, is justified by the extremely anomalous structure of the Nazca plate, which has surface heat flow values of ∼30 mW/m$^2$ compared to its theoretical 70 mW/m$^2$ (considering its 50 Ma age [*Springer and Forster*, 1998]). Furthermore, the fore-arc mantle into which the Nazca plate subducts is also probably cold and only partially serpentinized, as indicated by previously acquired geophys-

ical data such as Qp attenuation, magnetotellurics or shear wave splitting data. This generally cold state of the subduction zone may have significant implications on the kinetics of metamorphic reactions and on the rock structures. Although water saturated, the slab could display offsets between real parageneses and predicted ones estimated from equilibrium thermodynamics petrogenetic grids. This feature, together with the fact that north Chile DSZ most probably contains partially hydrated rock zones, suggests texturally heterogeneous environments in which rock fragments of metastable mineral assemblages (i.e., gabbro, peridotite) persist within metamorphic rocks of higher metamorphic grade (i.e., blueschist, eclogite) or more hydrated rocks (i.e., serpentinite). Global velocity properties of such environments could be strongly affected by this textural heterogeneity, such as Vp values being more sensitive to the water content of a weak matrix and Vs values being more sensitive to rigid nodules.

[81] 6. Thermomechanical models consistent with a cold environment reproduce the deformation and stress patterns of the subduction zone. In agreement with previous studies, deformation propagates from the subduction channel shear zone, into the Altiplano lower crust and the Subandean zone, whereas the fore-arc area remains rigid and sustains high stresses down into fore-arc mantle. When these thermomechanical models are superimposed on the seismic data, the DSZ is predicted to lie within the 350–450°C range that contours an inner slab compressional zone from 80 to 140 km depth. This cold temperature range is about 100°C lower than predictions from thermal models for other, yet probably warmer subduction zones. Alternate tests show that warmer slab and fore-arc conditions reduce the extent and intensity of this inner slab compressional zone.

[82] 7. From the thermomechanical models, lower plane earthquakes are predicted to occur in the neutral fiber plane between downdip tension and
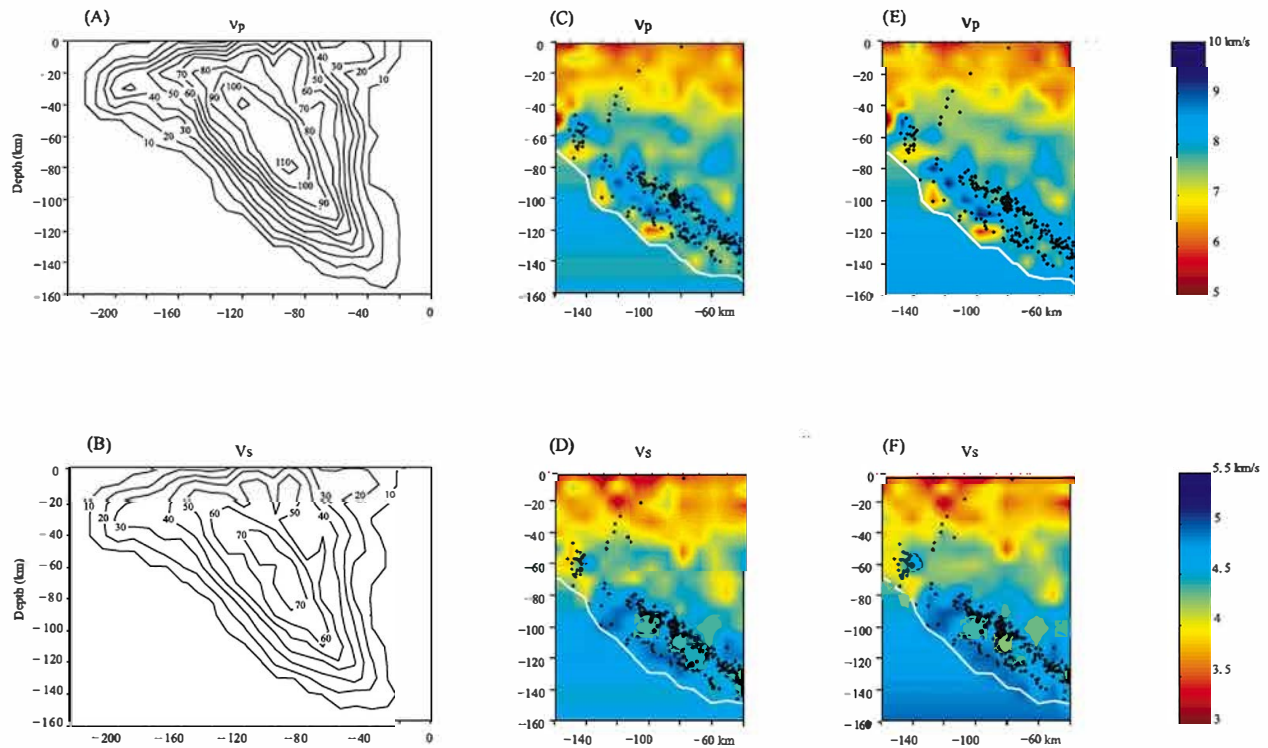
**Figure A1.** Checking the robustness of the solution. The square root of the derivative weight sum (DWS) (a) for P waves and (b) for S waves along profile P2. (c) Vp and (d) Vs models obtained starting from the final 1-D model (red dots, Figure 2). (e) Vp and (f) Vs models obtained starting from the initial model (blue dots, Figure 2). We see that the influence of the initial velocity model is minor.

downdip compression, where we suggest that fluids released from surrounding metamorphic reactions can migrate. We think that tensile stresses below this neutral plane open pores and favor upward migration of free fluids, whereas compressive stresses above this neutral plane closes pores and creates a permeability barrier able to trap fluids along a thinly sheeted serpentinized layer. This would be consistent with the generally admitted relation between dehydration reactions and seismicity [*Nakajima et al.*, 2001; *Takei*, 2002; *Hacker et al.*, 2003a]. Therefore these lower plane earthquakes are likely to present both downdip compression and downdip extension characteristics, precisely because of their location about the neutral plane. In between both seismic planes, the models produce compressional stresses of several hundreds MPa: this should affect seismic velocities, and in particular, reduce the amount of fluids required to explain observed values.

[83] 8. Numerical tests indicate that the inner slab compressional zone depends on the following parameters: (1) An older plate yields deeper isotherms and also deeper compressional zone. (2) A

weak ductile subduction channel favors inner slab compression, by facilitating transmission of compressional stresses from the upper plate. (3) A cold structure of the continental fore arc also favors inner slab compression, for the same reason. (4) Decreasing subducting plate radius of curvature broadens the inner slab compression upward and downward. (5) Decreasing upper plate convergence diminishes it. All these results indicate that if indeed DSZ's contours inner slab compression in general, they cannot only be linked to slab unbending (e.g., see discussion by *Abers* [1992]), but also to the transmission of compressional stresses from the upper plate into the slab, as *Fujita and Kanamori* [1981] suggested. In the case of Honshu and New Zealand, both subducting plates are much older than northern Chile, but display equivalent surface heat fluxes capable to create the appropriate cool environment for segmented compressional stresses to develop. Furthermore, if we apply *Brudzinsky et al.*'s [2007] rule of thumb of DSZ separations equal to 0.14 km/Ma, a plate age of 50 Ma should give a separation of 7 km. If we use an effective plate age of 100 Ma more consistent
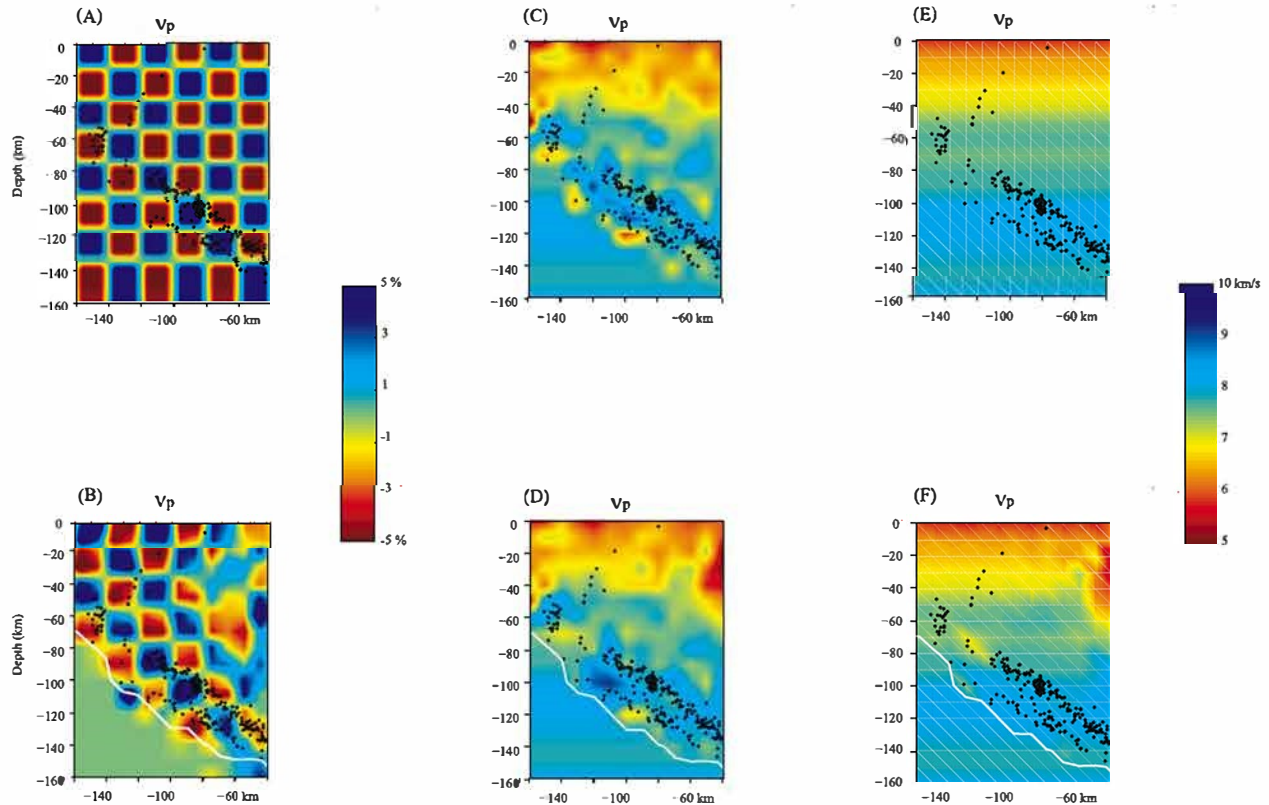
**Figure B1.** Three resolution tests performed to study the resolution of our inversion for **Vp**. Checkerboard test: (a) P wave input perturbation model, consisting of patches of two nodes with velocities ±5% compared to the normal starting model. (b) Recovered perturbation model. This test highlights the fine resolution of the features in the studied DSZ area. Restoring resolution test: (c) P wave input velocity model, which is the inverted true model. (d) Recovered velocity model. The velocity features in the subduction zone are well recovered in place and magnitude. This test shows that if the observed anomalies exist, the data set enables to recover them. Synthetic test of a velocity model without any velocity anomaly: (e) P wave input velocity model. (f) Recovered velocity model. This test shows that if no anomaly exists, our data do not generate it.

with the observed surface heat flow in northern Chile, then this separation should be 14 km, still lower than what is actually obtained in this study. Consequently, there must be another factor than plate age alone, that controls the distance between both seismic planes. The previous models indicate that indeed, the compressional state of stress of the upper plate transmits into the subducting plate, and increases the thickness and magnitude of its own compressional state, thus increasing the DSZ separation. Further global studies should help confirm this effect.

## Appendix A: Check of the Robustness of the Solution

[84] The square root of the derivative weight sum (DWS) along profile P2 (Figure 1) is presented for Vp and Vs models in Figures A1a and A1b, respectively. Thereafter, the isovalue 10, considered as the limit for resolved structures, is drawn on all figures. The influence of the chosen initial velocity model on the final velocity structures is presented in Figure A1. Figures A1c and A1d present the results obtained for Vp and Vs starting from the final 1-D model (red dots, Figure 2), whereas Figures A1e and A1f present the results obtained starting from the initial model (blue dots, Figure 2). We see that the influence of the initial velocity model is minor.

## Appendix B

[85] Three resolution tests are presented for Vp (Figure B1) and for Vs (Figure B2). In each test, the calculated synthetic absolute and differential

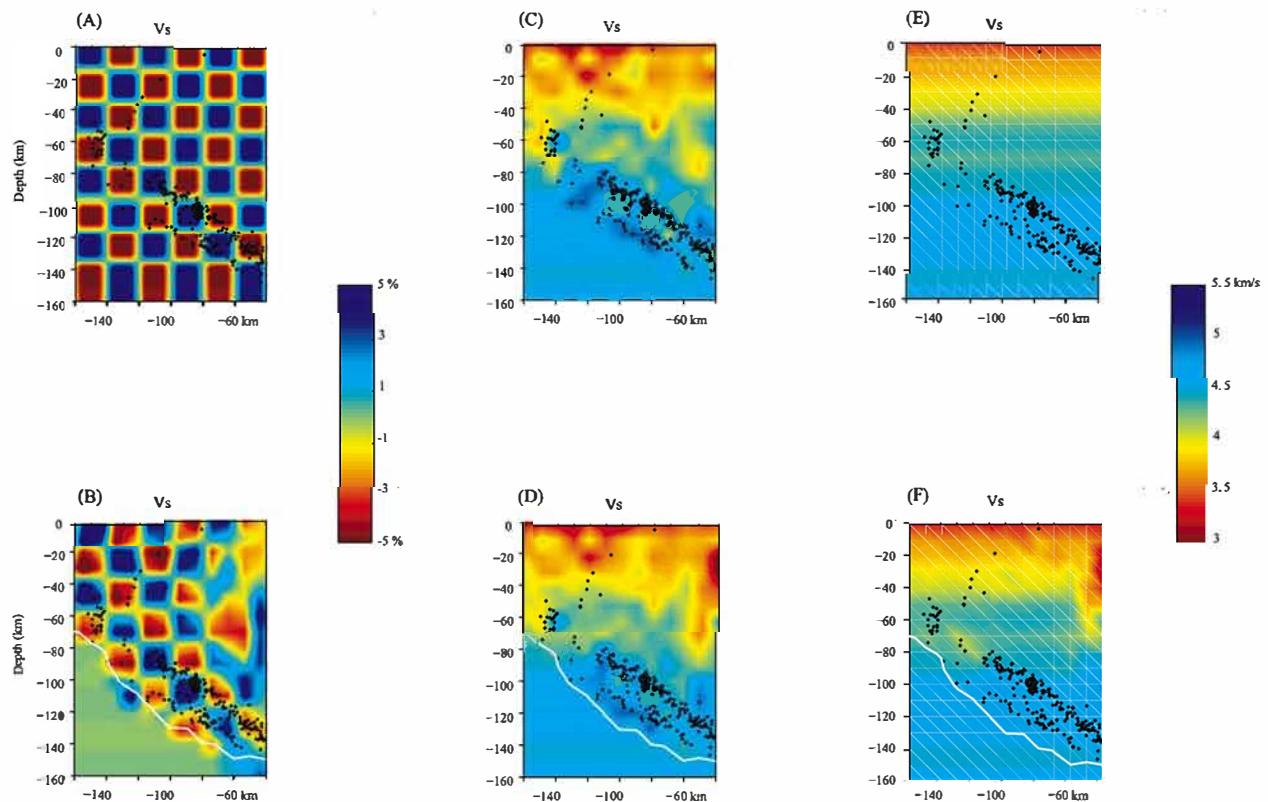**Figure B2.** (a–f) Same as Figure B1 for S waves.

travel times are included only for the same data distribution as for the real data. Following the standard procedure, we add uniformly distributed random noise to the synthetic data, in the interval ±0.025 s for P waves and ±0.05 s for S waves. The inverted models are obtained with the same inversion scheme as the real data set and starting from the same 1-D final model. Similar resolution tests have been performed in DSZ contexts by *Zhang et al.* [2004] or *Shelly et al.* [2006].

[86] 1. For the checkerboard test, the synthetic input P- and S-wave velocity models consist of 20 × 20 × 20 km patches (covering 2 nodes in horizontal and vertical directions) with velocities alternatively +5% and 5% compared to the normal starting model (Figures B1a and B2a). Recovered P and S wave models are presented in Figures B1b and B2b. It is clear that P and S wave velocities features are well resolved in the subduction zone. The features are recovered in position and magnitude for the upper plane, but with a bit lower amplitudes for the lower plane. In the test presented here, the diagonal step of the grid (45°) differs from the dip of the slab (35°), and the color alternance of diagonal high/low velocities, if sim-

ilar to our results for Vp, is opposite to our results for Vs. The continental lithosphere area is poorly resolved down to 80 km to the east, a result that is evident in both following tests.

[87] 2. The restoring resolution test [*Zhao et al.*, 1992] estimates the ability of the real data to recover the model obtained from the inversion. The input velocity models, which are the inverted true models, are shown in Figures B1c and B2c, and the corresponding recovered velocity models are shown in Figures B1d and B2d. The velocity features of the subduction zone are well recovered in position and magnitude within the upper plane. Within the lower plane, the recovered velocities are decreased. Nevertheless, this test shows that if the observed anomalies exist, the data set enables to recover them.

[88] 3. The last test starts from an input model without any velocity anomaly (Figures B1e and B2e). Except in the easternmost part of the recovered velocity models (Figures B1f and B2f), no marked anomaly is observed. This third test shows that if no anomaly exists, our data do not generate

it, therefore if no low Vp/high Vs zone is present, the inversion does not generate it as an artifact.

## Appendix C: Thermomechanical Markers Procedure for Tracking Pressure and Temperature

[89] Remeshing in Lagrangian methods is a common source of numerical diffusion, that the use of passive markers diminish, but cannot completely inhibit [e.g., *Yamato et al.*, 2007]. In Parovoz like in other FLAC methods [*Cundall and Board*, 1988], stresses and strains are computed at each time step on the triangle subelements of the mesh (each element is made of 2 superimposed pairs of triangles that allow accurate calculation of stress and strain components), and temperatures and velocities are nodal values). At the onset of the run, we inserted 9 regularly spaced markers in each mesh element, that passively move with the Lagrangian grid during normal computation, and carry linearly interpolated, elementary stresses and temperatures. All 9 markers of a same element are assigned identical element material properties, grouping density, conductivity, and rheological parameters, represented by a color "phase" in the setup in Figure 5. When the angle of any triangular element becomes smaller than a critical value, set to 13°here, remeshing occurs and a new regular mesh replaces the old one. Then, the markers are counted in each new element, in order to identify the dominant material properties ("phase") that composes it. During remeshing, markers are also used to evaluate subelement stress components (and therefore, pressure): new stress components are averaged over that of all markers located inside the new subelement. For temperature, new nodal and markers temperatures are linearly interpolated from the old nodal mesh.

[90] In Figure 8b, we plot markers of values in the pressure neutral plane of the slab (Plithos in green), and in the plane located 200 MPa above and below (Plithos + 200 MPa in blue and Plithos 200 MPa in red respectively), within a ±15 MPa range. Colored dots are markers, colored lines show averaged local values, and black lines indicate depth zone. We see that markers of a same color and at similar depths follow inclined straight patterns, that correspond to markers belonging to a same subelement: since pressure is an elementary value, markers thus have constant pressure, but slightly different lithostatic pressure because they are located at different depths (within the ±15 MPa interval). On the other hand, markers temperatures are interpolated from nodal values, and therefore do not present such artificially grouped patterns. We see that temperatures vary, at given depth, by about 20°C (horizontal extent of dots): this value is constrained by our choice of the ±15 MPa pressure interval. If we took a smaller pressure interval, then "holes" would appear at certain depths zones, because there would be no markers of that pressure range, in that zone. These "holes" are typically 2 to 3 km wide, equal to the mesh resolution there. At a given depth, the three colored lines show a relative pressure offset of 200 MPa (as prescribed), and a temperature difference of about 30°C, which is greater than the 20°C range that individuates each pressure range (width area of same color dots on Figure 8b). Consequently our mesh resolution allows to differentiate these three domains.

## Acknowledgments

## References

Abers, G. A. (1992), Relationship between shallow and inter mediate depth seismicity in the Eastern Aleutian subduction zone, *Geophys. Res. Lett.*, *19*, 2019 2022, doi:10.1029/92GL02060.

Abers, G. A., P. van Keken, E. A. Kneller, A. Ferris, and J. Stachnik (2006), The thermal structure of subduction zones constrained by seismic imaging: Implications for slab dehydration and wedge flow, *Earth Planet. Sci. Lett.*, *241*, 387 397, doi:10.1016/j.epsl.2005.11.055.

Beck, S. L., and G. Zandt (2002), The nature of orogenic crust in the central Andes, *J. Geophys. Res.*, *107*(B10), 2230, doi:10.1029/2000JB000124.

Benn, K., A. Nicolas, and I. Reuber (1988), Mantle crust transition zone and origin of wehrlitic magmas: Evidence from the Oman Ophiolite, *Tectonophysics*, *151*, 75 85, doi:10.1016/0040 1951(88)90241 7.

Billen, M. I., and M. Gurnis (2001), A low viscosity wedge in subduction zones, *Earth Planet. Sci. Lett.*, *193*, 227 236, doi:10.1016/S0012 821X(01)00482 4.

Brasse, H. (2005), The mantle wedge in the Bolivian orocline in the view of deep electromagnetic soundings, paper pre sented at 6th International Symposium on Andean Geody namics, Inst. de Rech. pour le Dev., Barcelona, Spain.

Brasse, H., P. Lezaeta, V. Rath, K. Schwalenberg, W. Soyer, and V. Haak (2002), The Bolivian Altiplano conductivity anomaly, *J. Geophys. Res.*, *107*(B5), 2096, doi:10.1029/2001JB000391.

Brudzinski, M. R., C. H. Thurber, B. R. Hacker, and R. E. Engdahl (2007), Global prevalence of double Benioff zones, *Science*, *316*, 1472 1474.

Burov, E. B., and M. Diament (1995), The effective elastic thickness of continental lithosphere: What does it really mean?, *J. Geophys. Res.*, *100*, 3905 3927, doi:10.1029/94JB02770.

Burov, E. B., and A. Poliakov (2001), Erosion and rheology controls on synrift and postrift evolution: Verifying old and new ideas using a fully coupled numerical model, *J. Geophys. Res.*, *106*, 16,461 16,481, doi:10.1029/2001JB000433.

Burov, E. B., C. Jaupart, and L. Guillou Frottier (2003), Ascent and emplacement of magma reservoirs in brittle ductile upper crust, *J. Geophys. Res.*, *108*(B4), 2177, doi:10.1029/2002JB001904.

Cande, S. C., and W. E. Haxby (1991), Eocene propagating rifts in the southwest Pacific and their conjugate features on the Nazca plate, *J. Geophys. Res.*, *96*, 19,609 19,622, doi:10.1029/91JB01991.

Carson, C. J., R. Powell, and G. L. Clarke (1999), Calculated mineral equilibria for eclogites in CaO Na$_2$O FeO MgO Al$_2$O$_3$ SiO$_2$ H$_2$O: Application to the Pouébo Terrane, Pam Peninsula, New Caledonia, *J. Metamorph. Geol.*, *17*, 9 24, doi:10.1046/j.1525 1314.1999.00177.x.

Ceuleneer, G., A. Nicolas, and F. Boudier (1988), Mantle flow patterns at an oceanic spreading centre: The Oman peridotites record, *Tectonophysics*, *151*, 1 26, doi:10.1016/0040 1951(88)90238 7.

Christensen, U. (1996), Poisson's ratio and crustal seismology, *J. Geophys. Res.*, *101*, 3139 3156, doi:10.1029/95JB03446.

Clarke, G. L., J. C. Aitchison, and D. Cluzel (1997), Eclogites and Blueschists of the Pam Peninsula, NE New Caledonia: A reappraisal, *J. Petrol.*, *38*, 843 876, doi:10.1093/petrology/38.7.843.

Clouard, V., J. Campos, A. Lemoine, A. Perez, and E. Kausel (2007), Outer rise stress changes related to the subduction of the Juan Fernandez Ridge, central Chile, *J. Geophys. Res.*, *112*, B05305, doi:10.1029/2005JB003999.

Coleman, R. G., and T. E. Keith (1971), A chemical study of serpentinisation, Burro Mountain, California, *J. Petrol.*, *12*, 311 328.

Comte, D., and G. Suarez (1994), An inverted double seismic zone in Chile: Evidence of phase transformation in the subducted slab, *Science*, *263*, 212 215, doi:10.1126/science.263.5144.212.

Comte, D., L. Dorbath, M. Pardo, T. Monfret, H. Haessler, L. Rivera, M. Frogneux, B. Glass, and C. Meneses (1999), A double layered seismic zone in Arica, northern Chile, *Geophys. Res. Lett.*, *26*, 1965 1968, doi:10.1029/1999GL900447.

Comte, D., J. Battaglia, C. Thurber, H. Zhang, L. Dorbath, and B. Glass (2004), High resolution subducting slab structure beneath northern Chile using the double difference method, *Eos. Trans. AGU*, *85*(47), Fall Meet. Suppl., Abstract S53B 0200.

Conder, J. A. (2005), A case for hot slab surface temperatures in numerical viscous flow models of subduction zones with improved fault zone parameterization, *Phys. Earth Planet. Inter.*, *149*, 155 164, doi:10.1016/j.pepi.2004.08.018.

Cundall, P., and M. Board (1988), A microcomputer program for modeling large strain plasticity problems, *Numer. Meth ods Geomech.*, *6*, 2101 2108.

Currie, C. A., and R. D. Hyndman (2006), The thermal structure of subduction zone back arcs, *J. Geophys. Res.*, *111*, B08404, doi:10.1029/2005JB004024.

DeMets, C., R. G. Gordon, D. F. Argus, and S. Stein (1990), Current plate motions, *Geophys. J. Int.*, *101*, 425 478, doi:10.1111/j.1365 246X.1990.tb06579.x.

Engdahl, E. R., and C. H. Scholz (1977), A double Benioff zone beneath the central Aleutians: An unbending of the lithosphere, *Geophys. Res. Lett.*, *4*, 473 476, doi:10.1029/GL004i010p00473.

Evans, B. W. (2004), The serpentinite multisystem revisited: Chrysotile is metastable, *Int. Geol. Rev.*, *46*, 479 506, doi:10.2747/0020 6814.46.6.479.

Fujita, K., and H. Kanamori (1981), Double seismic zones and stresses of intermediate depth earthquakes, *Geophys. J. R. Astron. Soc.*, *66*, 131 156.

Gerbault, M., S. Henrys, and F. Davey (2003), Numerical models of lithospheric deformation forming the Southern Alps of New Zealand, *J. Geophys. Res.*, *108*(B7), 2341, doi:10.1029/2001JB001716.

Graeber, M., and G. Asch (1999), Three dimensional models of P wave velocity and P to S velocity ratio in the southern central Andes by simultaneous inversion of local earthquake data, *J. Geophys. Res.*, *104*(B9), 20,237 20,256, doi:10.1029/1999JB900037.

Guiraud, M., T. Holland, and R. Powell (1990), Calculated mineral equilibria in the greenschist blueschisteclogite facies in Na$_2$O FeO MgO Al$_2$O$_3$ SiO$_2$ H$_2$O. Methods, results and geological applications, *Contrib. Mineral. Petrol.*, *104*, 85 98, doi:10.1007/BF00310648.

Haberland, C., A. Rietbrock, B. Schurr, and H. Brasse (2003), Coincident anomalies of seismic attenuation and electrical resistivity beneath the southern Bolivian Altiplano plateau, *Geophys. Res. Lett.*, *30*(18), 1923, doi:10.1029/2003GL017492.

Hacker, B. R., and G. A. Abers (2004), Subduction Factory 3: An Excel worksheet and macro for calculating the densities, seismic wave speeds, and H$_2$O contents of minerals and rocks at pressure and temperature, *Geochem. Geophys. Geosyst.*, *5*, Q01005, doi:10.1029/2003GC000614.

Hacker, B. R., G. A. Abers, and S. M. Peacock (2003a), Subduction factory 1. Theoretical mineralogies, densities, seismic wave speeds, and H$_2$O contents, *J. Geophys. Res.*, *108*(B1), 2029, doi:10.1029/2001JB001127.

Hacker, B. R., S. M. Peacock, G. A. Abers, and S. D. Holloway (2003b), Subduction factory 2: Are intermediate depth earthquakes in subducting slabs linked to metamorphic dehydration reactions?, *J. Geophys. Res.*, *108*(B1), 2030, doi:10.1029/2001JB001129.

Hamza, V. M., and M. Muñoz (1996), Heat flow map of South America, *Geothermics*, *25*(6), 599 646, doi:10.1016/S0375 6505(96)00025 9.

Hasegawa, A., N. Umino, and A. Takagi (1978), Double planed deep seismic zone and upper mantle structure in the northeastern Japan arc, *Geophys. J. R. Astron. Soc.*, *54*, 281 296.

Honda, S. (1985), Thermal structure beneath Tohoku, northeast Japan A case study for understanding the detailed thermal structure of the subduction zone, *Tectonophysics*, *112*, 69 102, doi:10.1016/0040 1951(85)90173 8.

Hyndman, R. D., and S. M. Peacock (2003), Serpentinization of forearc mantle, *Earth Planet. Sci. Lett.*, *212*, 417 432, doi:10.1016/S0012 821X(03)00263 2.

Isacks, B. L., and M. Barazangi (1977), Geometry of Benioff zones: Lateral segmentation and downwards bending of the subducted lithosphere, in *Island Arcs, Deep Sea Trenches, and Back Arc Basins*, *Maurice Ewing Ser.*, vol. 1, edited by M. Talwani and W. C. Pitman III, pp. 99 114, AGU, Washington, D. C.

Ji, S., and Z. Wang (1999), Elastic properties of forsterite enstatite composites up to 3.0 GPa, *J. Geodyn.*, *28*, 147 174, doi:10.1016/S0264 3707(98)00034 9.

Jung, H., H. W. Green, II and L. F. Dobrzhinetskaya (2004), Intermediate depth earthquake faulting by dehydration em brittlement with negative volume change, *Nature*, *428*, 545 549, doi:10.1038/nature02412.

Kelemen, P. B., J. L. Rilling, E. M. Parmentier, L. Mehl, and B. R. Hacker (2003), Thermal structure due to solid state flow in the mantle wedge beneath arcs, in *Inside the Sub duction Factory*, *Geophys. Monogr. Ser.*, vol. 138, edited by J. M. Eiler, pp. 293 311, AGU, Washington, D. C.

Kirby, S. H., E. R. Engdahl, and R. Denlinger (1996), Inter mediate depth intraslab earthquakes and arc volcanism as physical expressions of crustal and uppermost mantle meta morphism in subducting slabs, in *Subduction: Top to Bottom*, *Geophys. Monogr. Ser.*, vol. 96, edited by G. E. Bebout et al., pp. 195 214, AGU, Washington, D. C.

Kneller, E. A., P. E. van Keken, I. Katayama, S. Karato, and J. Park (2005), B type olivine fabric in the mantle wedge: Insights from high resolution non Newtonian subduction zone models, *Earth Planet. Sci. Lett.*, *237*, 781 797, doi:10.1016/j.epsl.2005.06.049.

Kneller, E. A., P. E. van Keken, I. Katayama, and S. Karato (2007), Stress, strain, and B type olivine fabric in the fore arc mantle: Sensitivity tests using high resolution steady state subduction zone models, *J. Geophys. Res.*, *112*, B04406, doi:10.1029/2006JB004544.

Lamb, S. (2006), Shear stresses on megathrusts: Implications for mountain building behind subduction zones, *J. Geophys. Res.*, *111*, B07401, doi:10.1029/2005JB003916.

Lamb, S. H., and P. Davis (2003), Cenozoic climate change as a possible cause for the rise of the Andes, *Nature*, *425*, 792 797, doi:10.1038/nature02049.

Lavier, L., W. Buck, and A. Poliakov (1999), Self consistent rolling hinge model for the evolution of large onset low angle normal faults, *Geology*, *27*, 1127 1130.

Le Pourhiet, L., E. Burov, and I. Moretti (2004), Rifting through a stack of inhomogeneous thrusts (the dipping pie concept), *Tectonics*, *23*, TC4005, doi:10.1029/2003TC001584.

Lucassen, F., R. Becchio, R. Harmon, S. Kasemann, G. Franz, R. Trumbull, R. L. Romer, and P. Dulski (2001), Composi tion and density model of the continental crust in an active continental margin The central Andes between 18° and 27°S, *Tectonophysics*, *341*, 195 223, doi:10.1016/S0040 1951(01)00188 3.

Nakajima, J., T. Matsuzawa, A. Hasegawa, and D. Zhao (2001), Three dimensional structure of Vp, Vs, and Vp/Vs beneath northeastern Japan: Implications for arc mgmatism and fluids, *J. Geophys. Res.*, *106*(B10), 21,843 21,858, doi:10.1029/2000JB000008.

Parsons, B., and J. G. Sclater (1977), An analysis of the variation of ocean floor bathymetry and heat flow with age, *J. Geophys. Res.*, *82*, 803 827, doi:10.1029/JB082i005p00803.

Peacock, S. M. (2001), Are the lower planes of double seismic zones caused by serpentinite dehydration in subducting ocea nic mantle?, *Geology*, *29*, 299 302, doi:10.1130/0091 7613(2001)029<0299:ATLPOD>2.0.CO;2.

Peacock, S. M., and K. Wang (1999), Seismic consequences of warm versus cool subduction metamorphism: Examples from southwest and northeast Japan, *Science*, *286*, 937 939, doi:10.1126/science.286.5441.937.

Perrillat, J. P., I. Daniel, K. T. Koga, B. Reynard, H. Cardon, and W. A. Crichton (2005), Kinetics of antigorite dehydra tion: A real time X ray diffraction study, *Earth Planet. Sci. Lett.*, *236*, 899 913, doi:10.1016/j.epsl.2005.06.006.

Poliakov, A., and Y. Podladchikov (1992), Diapirism and to pography, *Geophys. J. Int.*, *109*, 553 564, doi:10.1111/j.1365 246X.1992.tb00117.x.

Poliakov, A., H. J. Hermann, Y. Podladchikov, and S. Roux (1994), Fractal plastic shear bands, *Fractals*, *2*, 567 581, doi:10.1142/S0218348X9400079X.

Prince, R. A., and L. D. Kulm (1975), Crustal rupture and the initiation of imbricate thrusting in the Peru Chile Trench, *Geol. Soc. Am. Bull.*, *86*, 1639 1653, doi:10.1130/0016 7606(1975)86<1639:CRATIO>2.0.CO;2.

Ranalli, G. (1995), *Rheology of the Earth*, Chapman and Hall, London.

Reyners, M., D. Eberhart Phillips, G. Stuart, and Y. Nishimura (2006), Imaging subduction from the trench to 300 km depth beneath the central North Island, New Zealand, with Vp and Vp/Vs, *Geophys. J. Int.*, *165*, 565 583, doi:10.1111/j.1365 246X.2006.02897.x.

Rietbrock, A., and F. Waldhauser (2004), A narrowly spaced double seismic zone in the subducting Nazca plate, *Geophys. Res. Lett.*, *31*, L10608, doi:10.1029/2004GL019610.

Roperch, P., T. Sempere, O. Macedo, C. Arriagada, M. Fornari, C. Tapia, M. Garcia, and C. Laj (2006), Counterclockwise rotation of late Eocene Oligocene forearc deposits in south ern Peru and its significance for oroclinal bending in the central Andes, *Tectonics*, *25*, TC3010, doi:10.1029/2005TC001882.

Schilling, F. R., et al. (2006), Partial melting in the central Andean crust: A review of geophysical, petrophysical, and petrologic evidence, in *The Andes*, edited by O. Oncken et al., pp 459 474, Springer, Berlin.

Schurr, B., and A. Rietbrock (2004), Deep seismic structure of the Ata cama basin, northern Chile, *Geophys. Res. Lett.*, *31*, L12601, doi:10.1029/2004GL019796.

Seno, T., and Y. Yamanaka (1996), Double seismic zones, compressional deep outer rise events, and superplumes, in *Subduction: Top to Bottom*, *Geophys. Monogr. Ser.*, vol. 96, edited by G. E. Bebout et al., pp. 347 355, AGU, Washington, D. C.

Shelly, D. R., G. C. Beroza, H. Zhang, C. H. Thurber, and S. Ide (2006), High resolution subduction zone seismicity and velocity structure beneath Ibaraki Prefecture, Japan, *J. Geophys. Res.*, *111*, B06311, doi:10.1029/2005JB004081.

Sleep, N. H. (1979), The double seismic zone in downgoing slabs and the viscosity of the mesosphere, *J. Geophys. Res.*, *84*, 4565 4571, doi:10.1029/JB084iB09p04565.

Sobolev, S. V., and A. Y. Babeyko (2005), What drives oro geny in the Andes?, *Geology*, *33*(8), 617 620, doi:10.1130/G21557.1.

Sobolev, S. V., and A. Y. Babeyko (2006), Modeling subduc tion of the continental crust at the Andean type convergent margin, *Geochim. Cosmochim. Acta*, *70*(18), A601, doi:10.116/j.gca.2006.06.1116.

Springer, M. (1999), Interpretation of heat flow density in the central Andes, *Tectonophysics*, *306*, 377 395, doi:10.1016/S0040 1951(99)00067 0.

Springer, M., and A. Forster (1998), Heat flow density across the central Andean subduction zone, *Tectonophysics*, *291*, 123 139, doi:10.1016/S0040 1951(98)00035 3.

Syracuse, E. M., and G. A. Abers (2006), Global compilation of variations in slab depth beneath arc volcanoes and implications, *Geochem. Geophys. Geosyst.*, *7*, Q05017, doi:10.1029/2005GC001045.

Takazawa, E., T. Okayasu, and K. Sahoh (2003), Geochemistry and origin of the basal lherzolites from the northern Oman Ophiolite (northern Fizh Block), *Geochem. Geophys. Geosyst.*, *4*(2), 8605, doi:10.1029/2001GC000232.

Takei, Y. (2000), Acoustic properties of partially molten media studied on a simple binary system with a controllable dihedral angle, *J. Geophys. Res.*, *105*, 16,665 16,682, doi:10.1029/2000JB900124.

Takei, Y. (2002), Effect of pore geometry on Vp/Vs: From equilibrium geometry to crack, *J. Geophys. Res.*, *107*(B2), 2043, doi:10.1029/2001JB000522.

Tassara, A. (2005), Interaction between the Nazca and South American plates and formation of the Altiplano Puna plateau: Review of a flexural analysis along the Andean margin (15° 34°S), *Tectonophysics*, *399*, 39 57, doi:10.1016/j.tecto.2004.12.014.

Tassara, A. (2006), Factors controlling the crustal density structure underneath active continental margins with implications for their evolution, *Geochem. Geophys. Geosyst.*, *7*, Q01001, doi:10.1029/2005GC001040.

Tassara, A., H. J. Götze, S. Schmidt, and R. Hackney (2006), Three dimensional density model of the Nazca plate and the Andean continental margin, *J. Geophys. Res.*, *111*, B09404, doi:10.1029/2005JB003976.

Tassara, A., C. Swain, R. Hackney, and J. Kirby (2007), Elastic thickness structure of South America estimated using wavelets and satellite derived gravity data, *Earth Planet. Sci. Lett.*, *253*, 17 36, doi:10.1016/j.epsl.2006.10.008.

Thurber, C. H. (1983), Earthquake locations and three dimensional crustal structure in the Coyote Lake area, central California, *J. Geophys. Res.*, *88*, 8226 8236, doi:10.1029/JB088iB10p08226.

Thurber, C. H. (1993), Local earthquake tomography: Velocities and Vp/Vs theory, in *Seismic Tomography: Theory and Practice*, edited by H. M. Iyer and K. Hirahara, pp. 563 583, Chapman and Hall, London.

Turcotte, D., and G. Schubert (1982), *Geodynamics: Applications of Continuum Physics to Geological Problems*, John Wiley, New York.

van Keken, P. E., B. Kiefer, and S. M. Peacock (2002), High resolution models of subduction zones: Implications for mineral dehydration reactions and the transport of water into the deep mantle, *Geochem. Geophys. Geosyst.*, *3*(10), 1056, doi:10.1029/2001GC000256.

Waldhauser, F. (2001), hypoDD: A computer program to compute double difference hypocenter locations, *U.S. Geol. Surv. Open File Rep. 01 113*, 25 pp.

Wang, K. (2002), Unbending combined with dehydration embrittlement as a cause for double and triple seismic zones, *Geophys. Res. Lett.*, *29*(18), 1889, doi:10.1029/2002GL015441.

Watanabe, T. (1993), Effects of water and melt on seismic velocities and their application to characterization of seismic reflectors, *Geophys. Res. Lett.*, *20*, 2933 2936, doi:10.1029/93GL03170.

Yamasaki, T., and T. Seno (2003), Double seismic zone and dehydratation embrittlement of the subducting slab, *J. Geophys. Res.*, *108*(B4), 2212, doi:10.1029/2002JB001918.

Yamato, P., P. Agard, E. Burov, L. Le Pourhiet, L. Jolivet, and C. Tiberi (2007), Burial and exhumation in a subduction wedge: Mutual constraints from thermomechanical modeling and natural P T t data (Schistes Lustrés, western Alps), *J. Geophys. Res.*, *112*, B07410, doi:10.1029/2006JB004441.

Zhang, H. (2003), Double difference seismic tomography method and its application, Ph.D. thesis, 189 pp., Univ. of Wisc. Madison, Madison.

Zhang, H., and C. H. Thurber (2003), Double difference tomography: The method and its application to the Hayward Fault, California, *Bull. Seismol. Soc. Am.*, *93*(5), 1875 1889, doi:10.1785/0120020190.

Zhang, H., C. H. Thurber, D. Shelly, S. Ide, G. C. Beroza, and A. Hasegawa (2004), High resolution subducting slab structure beneath northern Honshu, Japan, revealed by double difference tomography, *Geology*, *32*(4), 361 364, doi:10.1130/G20261.2.

Zhao, D., A. Hasegawa, and S. Horiuchi (1992), Tomographic imaging of P and S wave velocity structure beneath northeastern Japan, *J. Geophys. Res.*, *97*, 19,909 19,928, doi:10.1029/92JB00603.